

Possible Nature of Nonideal Perturbations Limiting Plasma Pressure in Tokamaks*

A. B. Mikhailovskii^{1,2}, A. P. Churikov³, S. V. Konovalov^{1,4},
M. S. Shirokov^{1,5}, and V. S. Tsypin⁶

Presented by Academician A.A. Fridman October 8, 2002

Received October 14, 2002

In this paper, we show that there exists a new class of perturbations limiting the pressure of ideally stable plasma in tokamak-type fusion reactors. Localization of such modes involves three characteristic regions, namely, large-scale magnetohydrodynamic (MHD), Larmor, and sub-Larmor ones. It is suggested that these modes can be responsible for spontaneous generation of neoclassical tearing modes observed experimentally.

1. Neoclassical tearing modes (NTMs) are considered to be one of the main obstacles in attaining acceptable values of the parameter β characterizing the ratio of the plasma pressure to the magnetic-field pressure in fusion reactors of the tokamak type [1]. The existing theory of NTMs [2] is based on the notion that these modes are excited by certain types of MHD activity such as edge-localized modes, sawtooth modes, and fishbones. Meanwhile, the experimental data from ASDEX Upgrade [3] and TFTR [4] facilities show that NTMs can be generated spontaneously, i.e., in the

absence of any MHD activity. To explain spontaneous generation of NTMs, we should appeal to a linear instability excited when the parameter β of ideally stable plasma exceeds a certain threshold value. However, the existing linear theory [5] fails to predict this instability.

The need to know the nonideal instability excited when the parameter β exceeds the threshold value is also required for explanation of experimental data on NTMs obtained from a series of tokamaks such as T-10 [6] with hot-electron plasma (plasma with the electron temperature substantially higher than the ion temperature). This is associated with the fact that, after the revision of the traditional NTM theory [7], it became clear that the polarization-current effect in such a plasma is destabilizing. Therefore, the revised theory predicts no threshold value of β for the NTM onset in these devices.

In principle, preceding theoretical investigations of linear modes in tokamaks include certain indications in favor of the existence of β -limiting instabilities. Thus, it was shown in [8] that, for $q \approx 1$ (q is the safety factor), an instability distorting the magnetic surfaces of tokamak-type toroidal systems can be excited in the case when (cf. Eq. (3.29) of [8])

$$\beta_p > \beta_p^{(0)} \equiv \frac{s^2 L_p^2}{r_s^2}. \quad (1)$$

Here, β_p is the poloidal β parameter, s is the shear, L_p is the characteristic scale of the plasma-pressure gradient, and r_s is the radial coordinate of the rational magnetic surface in which the mode is localized. According to [8], for excitation of this instability, the existence of a temperature gradient is necessary, which is similar to the case of instabilities of high-pressure plasma in a straight-line magnetic field [9].

In [8], the local approximation was used, which is insufficient to prove the existence of eigenmodes. This defect of [8] has been corrected in [10, 11]. The eigenmodes found in [10, 11] have been called beta-induced temperature-gradient (BTG) eigenmodes. The results of experimental observation of the BTG modes in the JET facility were reported in [12].

* This article was submitted by the authors in English.

¹ Institute of Nuclear Fusion,
Russian Research Centre Kurchatov Institute,
pr. Kurchatova 16, Moscow, 123182 Russia
e-mail: mikh@nfi.kiae.ru; konoval@nfi.kiae.ru

² Moscow Institute of Physics and Technology,
Institutskii per. 9, Dolgoprudnyĭ, Moscow oblast,
141700 Russia

³ Samara Technical University, Syzran' Division,
Syzran', Sovetskaya ul. 45, Samarskaya oblast,
446000 Russia
e-mail: apch@dtc.syzran.ru

⁴ Japan Atomic Energy Research Institute,
Naka Fusion Research Establishment, Naka-machi,
Naka-gun, Ibaraki-ken, 311-0193, Japan
e-mail: konoval@fusion.naka.jaeri.go.jp

⁵ Moscow Engineering Physics Institute,
Kashirskoe sh. 31, Moscow, 115409 Russia
e-mail: shirokovmephi@yandex.ru

⁶ Institute of Physics, University of São Paulo,
Rua do Matão, S/N, 05508-900 SP, Brazil
e-mail: tsypin@fap01.if.usp.br

It was assumed in [8, 10, 11] that the BTG modes are excited due to the toroidal acoustic resonance, i.e., are governed by the condition $\omega_* \approx \frac{v_{Ti}}{qR}$, where ω_* is the characteristic diamagnetic drift frequency, v_{Ti} is the ion thermal velocity, and R is the torus major radius. Such a resonance is efficient only for sufficiently high poloidal m and toroidal n mode numbers, namely, $m = nq \approx \frac{L_p r_s}{qR\rho_i} > 1$, where ρ_i is the ion Larmor radius. However, for NTM theory, perturbations with $m, n \approx 1$ are important.

The analysis performed in [8, 10, 11] was based on the approximation that the characteristic radial scale of the mode is sufficiently large, i.e., $k_x \rho_i \ll 1$, $k_x \rho_s \ll 1$. Here, ρ_s is the ion Larmor radius calculated from the electron temperature and k_x is the radial projection of the wave vector (the variable x is defined by the relationship $x = r - r_s$). Nevertheless, in order to reveal the eigenmodes, the authors of [10, 11] were forced to allow for formally small terms on the order of $(k_x \rho_i)^2$ and $(k_x \rho_s)^2$.

The goal of the present paper consists in the further development of the theory of linear instabilities in tokamaks with a finite value of β_p . Then, the existence of the perturbations covering the gap in the interpretation of experimental data on NTMs is demonstrated.

2. In addition to the theory of BTG modes, the theory of so-called semicollisional modes was developed [5, 13, 14]. These modes differ from the standard MHD modes by the fact that their perturbed electromagnetic field, being essential for $k_x \rho_i \ll 1$ and $k_x \rho_s \ll 1$, is also extended to sub-Larmor scales, i.e., to scales with $k_x \rho_i \geq 1$, $k_x \rho_s \geq 1$. In this theory, the eigenvalues are characterized by a dimensionless parameter v , which, in the particular case of plasma with the same equilibrium ion and electron temperatures $T_{0i} = T_{0e} = T_0$, is given by the formula

$$v^2 = \frac{1}{4} - \frac{(\omega - \omega_{*e})(\omega - \omega_{*i})}{2k_y^2 \rho_i^2 \omega_A^2}. \quad (2)$$

Here, ω is the perturbation frequency; $\omega_A = \frac{sv_A}{qR}$ is the Alfvén frequency; v_A is the Alfvén velocity; ω_{*e} and ω_{*i} are the electron and ion diamagnetic drift frequencies, respectively; and $k_y = \frac{m}{r_s}$ is the poloidal projection of the wave vector. According to [5], the parameter v

satisfies the dispersion relation [see (24.33) in [5]]

$$\frac{\Gamma^2\left(-\frac{1}{4} + \frac{v}{2}\right)\Gamma^2(-v)Q(v)}{\Gamma^2\left(-\frac{1}{4} - \frac{v}{2}\right)\Gamma^2(v)Q(-v)} = \left(\frac{4\kappa}{\hat{\beta}^2}\right)^v. \quad (3)$$

Furthermore, Γ is the gamma function,

$$Q(v) = 1 + \frac{\kappa^{-1/2} \Gamma^2\left(-\frac{1}{4} - \frac{v}{2}\right)}{8r_s \Delta' \Gamma^2\left(\frac{5}{4} - \frac{v}{2}\right)} \left(v^2 - \frac{1}{4}\right), \quad (4)$$

$$\kappa = \frac{2k_y^2 \rho_i^2}{1 - \frac{\omega_{*e}}{\omega}}, \quad (5)$$

$$\hat{\beta} = \frac{[-i(\omega - \omega_{*i})\gamma_R]^{1/2}}{2^{1/2} k_y \rho_i \omega_A}, \quad (6)$$

Δ' is the standard parameter of the tearing-mode theory, $\gamma_R = \frac{c^2 k_y^2}{4\pi\sigma}$ is the characteristic resistive decay rate, σ is the plasma electric conductivity, and c is the speed of light.

Until now, the analysis of dispersion relation (3) was performed only for the particular case $\left|v^2 - \frac{1}{4}\right| \ll 1$. In this case, this relation describes the semicollisional internal kink and tearing modes [13] and the semicollisional ballooning modes [14]. None of these modes belongs to the class of pressure-limiting modes.

In contrast to [13, 14], we consider the modes with ultimately small values of v , $v \rightarrow 0$. Then, we can see that dispersion relation (3) has the exact solution

$$v = 0. \quad (7)$$

It follows from (2) and (7) that

$$(\omega - \omega_{*e})(\omega - \omega_{*i}) - \frac{2\omega_{*e}^2 \beta_p^{(0)}}{\beta_p} = 0. \quad (8)$$

We call the modes described by (8) the ‘‘MHD–sub-Larmor’’ modes. They have the frequencies

$$\omega = \pm |\omega_*| \left(1 + 2 \frac{\beta_p^{(0)}}{\beta_p}\right)^{1/2}. \quad (9)$$

Here, we allow for $\omega_{*e} = -\omega_{*i} = -\omega_*$ at $T_{0e} = T_{0i}$.

According to (9), in the case of sufficiently low β_p , $\beta_p \ll \beta_p^{(0)}$, the mode frequencies turn out to be substantially larger than both the electron and ion diamagnetic drift frequencies. Therefore, in this case, the modes cannot be excited by electron or ion dissipative diamag-

netic drift effects. However, with increasing β_p , mode frequencies (9) decrease and turn out to be on the order of ω_{*e} or ω_{*i} under validity of condition (1) (see Fig. 1). For such β_p , the dissipative electron/ion drift effects can excite the modes under consideration.

3. We now show that the dispersion relation of type (3) can also be obtained in the case of vanishing ion temperature $\frac{T_{0i}}{T_{0e}} \rightarrow 0$. Similarly to Section 24.1 of [5], we start from the electric-current continuity equation written out in the Fourier space k_x and represent the contribution of the transverse current into this equation in the form

$$\nabla_{\perp} \cdot \mathbf{j}_{\perp} = -\frac{i\omega}{4\pi} k_x^2 \varepsilon_{\perp} \phi. \quad (10)$$

Here, ϕ is the electrostatic potential, $\varepsilon_{\perp} = \frac{c^2 f}{V_A^2}$ is the

transversal plasma permittivity, $f = f(\omega)$ is the toroidal renormalization of the transverse inertia [5], \mathbf{j}_{\perp} is the perturbed electric-current density, and ∇_{\perp} is the transverse gradient. Furthermore, we follow the approach proposed in Chapter 24 of the book [5]. The essence of this procedure consists in the fact that solutions are sought in the regions in which $k_x \rho_s \ll 1$, $k_x \rho_s \approx 1$, and $k_x \rho_s \gg 1$ (large-scale, Larmor, and sub-Larmor solutions). The unified solution is then constructed by the method of double asymptotic matching. As a result, we arrive at dispersion relation (3) with $Q(v)$ of form (4), where, in contrast to (2), (5), and (6), we now have

$$v^2 = \frac{1}{4} - \frac{\omega(\omega - \omega_{*e})}{k_y^2 \rho_s^2 \omega_A^2}, \quad (11)$$

$$\kappa = \frac{f k_y^2 \rho_s^2}{1 - \frac{\omega_{*e}}{\omega}}, \quad (12)$$

$$\hat{\beta} = \frac{(-i\omega\gamma_R)^{1/2}}{k_y \rho_s \omega_A}. \quad (13)$$

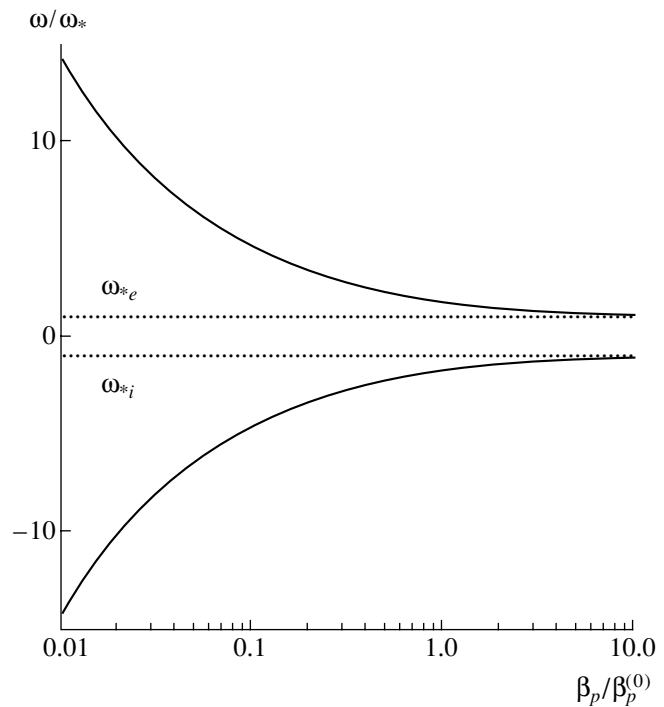
Then we again arrive at dispersion relation (7). However, instead of (8), we now have

$$\omega(\omega - \omega_{*e}) = \frac{1}{4} k_y^2 \rho_s^2 \omega_A^2. \quad (14)$$

Correspondingly, instead of (9), we obtain

$$\omega = \omega_{\pm} = -\frac{\omega_{*e}}{2} \left[1 \pm \left(1 + \frac{2s^2 L_n^2}{\beta_p r_s^2} \right)^{1/2} \right]. \quad (15)$$

As is seen, under condition (1), the modes propagating towards the electron-drift direction have frequencies on the order of electron diamagnetic-drift frequency. In



Frequency of MHD-sub-Larmor modes as a function of plasma pressure.

this case, perturbations can be excited by dissipative electron diamagnetic-drift effects.

4. Previously, in order to determine β_{crit} , one appealed to the polarization-current threshold model of NTMs [2]. As was said above, this model is inadequate for plasma in the case of $T_{0e} \gg T_{0i}$. Generally speaking, it is possible also to appeal to the transport threshold model of NTMs [15]. However this model contains coefficients of the anomalous transverse transport. Their values should be taken from experiment, which is rather problematic. Therefore, although in the framework of the transport model one can interpret experimental data obtained from certain particular devices, the possibility of satisfactorily interpreting in this manner the totality of experimental data seems doubtful. In this context, the concept of the generation of the indicated MHD-sub-Larmor modes [Eq. (20)] is an alternative to both the polarization-current and transport models in determining the value of β_{crit} .

ACKNOWLEDGMENTS

We are grateful to S.E. Sharapov for numerous useful discussions and comments. This work was supported by the Russian Foundation for Basic Research (project nos. 03-02-16294 and 00-15-96526, the latter is under the Russian Federal Program of Supporting Leading Scientific Schools), by the US Civilian Research and Development Foundation for the Independent States of the Former Soviet Union (grant BRHE REC-011), by the Research Support Foundation

of the State of São Paulo (FAPESP), University of São Paulo, and by the Excellence Research Programs (PRONEX), RMOC 50/70 grant of the Ministry of Science and Technology, Brazil.

REFERENCES

1. ITER Physics Expert Group on Disruptions, Plasma Control, and MHD, ITER Physics Basis Editors, Nucl. Fusion **39**, 2251 (1999).
2. H. R. Wilson, V. Alexander, and J. W. Connor, Plasma Phys. Controlled Fusion **38**, A149 (1996).
3. A. Gude, S. Gunter, and S. Sesnic, Nucl. Fusion **39**, 127 (1999).
4. E. D. Fredrickson, Phys. Plasmas **9**, 548 (2002).
5. A. B. Mikhaĭlovskiĭ, *Instabilities in a Confined Plasma* (Inst. Phys., Bristol, 1998).
6. D. A. Kislov *et al.* (T-10 Team), Nucl. Fusion **41**, 1619 (2001).
7. A. B. Mikhaĭlovskiĭ, V. D. Pustovitov, A. I. Smolyakov, and V. S. Tsypin, Phys. Plasmas **7**, 1214 (2000).
8. A. B. Mikhaĭlovskiĭ, Nucl. Fusion **13**, 259 (1973).
9. A. B. Mikhaĭlovskiĭ and A. M. Fridman, Zh. Éksp. Teor. Fiz. **51**, 1430 (1996) [Sov. Phys. JETP **24**, 965 (1967)].
10. A. B. Mikhaĭlovskiĭ and S. E. Sharapov, Fiz. Plazmy **25**, 872 (1999) [Plasma Phys. Rep. **25**, 803 (1999)].
11. A. B. Mikhaĭlovskiĭ and S. E. Sharapov, Fiz. Plazmy **25**, 911 (1999) [Plasma Phys. Rep. **25**, 838 (1999)].
12. S. E. Sharapov *et al.*, in *Proceedings of International Varenna-Lausanne Workshop on Fusion Plasmas, Varenna, 1998* (Compositori, Bologna, 1998), p. 215.
13. F. Pegoraro and T. J. Schep, Plasma Phys. Controlled Fusion **28**, 647 (1986).
14. A. B. Mikhaĭlovskiĭ, S. V. Novakovskiĭ, and A. P. Churikov, Fiz. Plazmy **14**, 914 (1988) [Sov. J. Plasma Phys. **14**, 536 (1988)].
15. S. V. Konovalov, A. B. Mikhaĭlovskiĭ, M. S. Shirokov, and V. S. Tsypin, Plasma Phys. Controlled Fusion **44**, L51 (2002).

Detonation of Emulsion Explosives Containing Hollow Microspheres

A. A. Deribas, A. E. Medvedev*, A. Yu. Reshetnyak,
and Corresponding Member of the RAS V. M. Fomin

Received January 9, 2003

INTRODUCTION

The absence of a theory of the detonation of emulsion explosives containing hollow microspheres stimulates us to write this paper. Results of calculations concerning the detonation of emulsion explosives differ considerably from the corresponding experimental data. The obvious disagreement between theoretical results and experimental data taken from [1] is seen in Fig. 1.

EXPERIMENT

The experiments were carried out with an emulsion explosive based on an aqueous solution of ammonium nitrate with hollow microspheres as an inert admixture. This admixture consisted of either ash microspheres (waste of a heat and electric power plant) sorted according to their sizes and apparent density or industrially produced glass microspheres.

Figure 2 shows the detonation velocity D measured for microspheres with various specific surface areas $S = n_{mb}d_{mb}^2$, where n_{mb} is the number of microspheres per unit charge volume and d_{mb}^2 is the initial diameter of microspheres.

SIMPLE MODEL OF THE DETONATION OF EMULSION EXPLOSIVES

According to the proposed model of the detonation of the emulsion explosive, the shells of microspheres break down behind the propagating shock front. As a result, gas in the microspheres is adiabatically compressed so that its pressure and temperature increase. Thus, the compressed microspheres represent hot spots for the initiation of a chemical reaction in the emulsion

base. The reaction front propagates spherically from each compressed microsphere as emulsion is heated. When a sphere expands up to the radius L_{ch} , the reaction terminates, because emulsion includes an inert component (water), the burning rate of combustible components in the products of ammonium-nitrate disintegration is low, and the rate of heat transfer from the heated gas to the emulsion is finite.

Thus, heat release behind the front of the leading shock wave is determined by the total heat release in all reacting spheres. It is this heat release that determines the detonation velocity in the emulsion explosive. At a low initial microsphere concentration, the heat release is low and, therefore, the detonation velocity is also low. At a sufficiently high microsphere concentration, the detonation velocity reaches its maximum. A further increase in the microsphere concentration leads to a decrease in the detonation velocity, because the amount of the emulsion base becomes insufficient for combustion (combustion spheres overlap) and the porosity of the explosive composition increases.

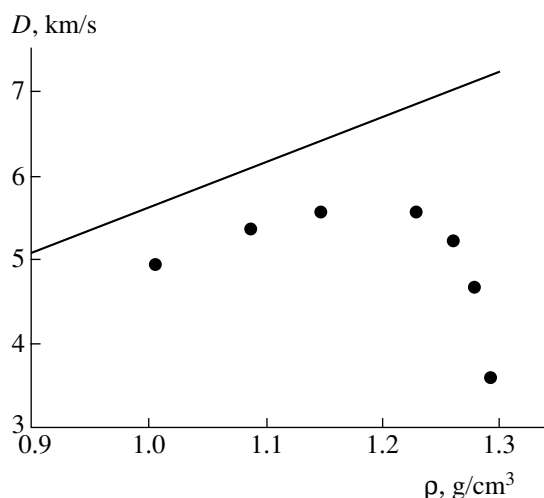


Fig. 1. Detonation velocity of the emulsion explosive vs. the emulsion density. Experimental data are taken from [1] and the line is calculated by the BKW code [1].

Institute of Theoretical and Applied Mechanics,
Siberian Division, Russian Academy of Sciences,
ul. Institutskaya 4/1, Novosibirsk, 630090 Russia
* e-mail: medvedev@itam.nsc.ru

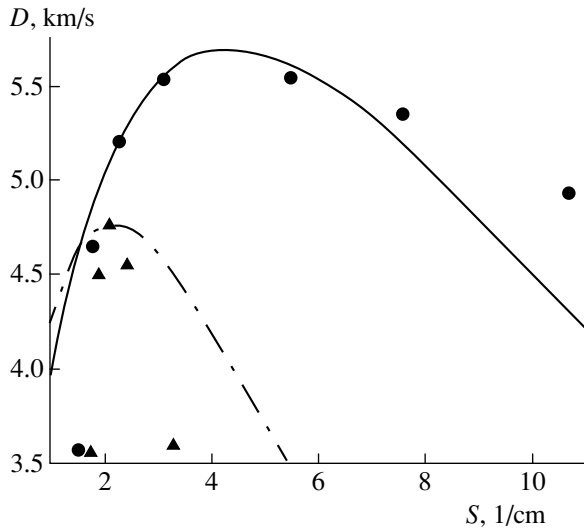


Fig. 2. Detonation velocity vs. the specific surface area of microspheres. Triangles are data for the emulsion explosive, which has an emulsion-base density of 1.35 g/cm³ and contains 125–160 μm diameter microspheres with the apparent density of 0.39 g/cm³; circles are data taken from [1]; and solid and dash-dotted lines are the detonation velocity calculated by model (2).

A mathematical formulation of the problem is presented below. It is obvious that $\rho_{mb} < \rho_0 \leq \rho_e$, where ρ_e is the emulsion-base density, ρ_{mb} is the actual microsphere density, and ρ_0 is the initial emulsion-explosive density. In terms of these parameters, the weight fraction of the microspheres in the emulsion and the porosity are expressed as $x_{mb} = \frac{\rho_{mb}(\rho_e - \rho_0)}{\rho_0(\rho_e - \rho_{mb})}$ and $K = \frac{\rho_e}{\rho_0}$, respectively. Then, the Chapman–Jouguet detonation velocity in the emulsion explosive is determined by the formula

$$D = K^{-\frac{n-1}{2}} \sqrt{2(\gamma^2 - 1)(1 - x_{mb})Q}. \quad (1)$$

RESULTS AND DISCUSSION

The detonation of emulsion explosives based on an aqueous solution of ammonium nitrate with hollow microspheres as a filler occurs through the mechanism of hot spots. Since the calorific value of the aqueous solution of ammonium nitrate is low, the combustion

reaction is quenched at a finite distance from the initiation point. The model proposed above takes into account the basic features of the detonation of emulsion explosives and shows that the classical conception of the detonation process (the Chapman–Jouguet model) provides qualitatively incorrect results (Fig. 1). The model ignores both the dependence of the detonation velocity on the diameter of the cylindrical charge and the properties of the microspheres (material, shell thickness, etc.). In addition, *a priori* determination of

$$Q = n_{nb} \frac{\pi}{6} L_{ch}^3 q, \quad n_{mb} = \frac{6m_{mb}}{\pi d_{mb}^3},$$

where $m_{mb} = \frac{x_{mb}\rho_0}{\rho_{mb}}$ is the volume fraction of the microspheres in the emulsion and q is the heat release of the reaction per unit mass of the emulsion base.

To express the detonation velocity D as a function of the specific surface area S , we find

$$\rho_0 = \rho_{mb}[1 - \alpha(\beta - 1)S],$$

where $\alpha = \frac{\pi}{6} d_{mb}$ and $\beta = \frac{\rho_e}{\rho_{mb}}$.

Then, Eq. (1) takes the form

$$D = \left[\frac{\beta}{\beta - \alpha(\beta - 1)S} \right]^{-\frac{n-1}{2}} \times \sqrt{AS \frac{\alpha\beta}{\beta - 1} \left[1 - \frac{1}{\beta - \alpha(\beta - 1)S} \right]}, \quad (2)$$

where $A = 2(\gamma^2 - 1)q \left(\frac{L_{ch}}{d_{mb}} \right)^3$.

The function $D = D(S)$ vanishes at the points $S_1 = 0$ and $S_2 = \frac{1}{\alpha}$ and reaches its maximum at

$$S_{max} = \frac{(n + 1)\beta - (n - 1) - \sqrt{(\beta + 1)^2 + (n - 1)^2 + n(n - 2)(\beta - 2)\beta - 1}}{2n\alpha(\beta - 1)}.$$

Figure 2 shows experimental data along with the calculations by model (2).

Figure 2 shows experimental data along with the calculations by model (2).

the constants A and n requires further investigation. Nevertheless, the model adequately describes the characteristic behavior of the detonation velocity (existence of its maximum, see Fig. 2) and qualitatively explains the processes.

ACKNOWLEDGMENTS

This work was supported by the Russian Foundation for Basic Research, project no. 02-01-01270.

REFERENCES

1. J. Lee and P. A. Persson, *Propellants, Explos., Pyrotech.* **15**, 208 (1990).
2. E. I. Zababakhin, *Some Questions of Explosion Gas Dynamics* (RFYaTs-VNIINTF, Snezhinsk, 1997).

Translated by Yu. Verevochkin

On the Ultrafast Synchronization of Oscillations in a Distributed Active Medium Formed by a Helical Electron Beam and a Counterpropagating Electromagnetic Wave

A. A. Koronovskii, Corresponding Member of the RAS D. I. Trubetskov, and A. E. Khramov

Received November 4, 2002

Nowadays, problems related to synchronization of self-oscillations in distributed self-oscillatory systems of an electronic nature have become of urgent interest from different points of view. Analysis of these problems is important from both the standpoint of fundamental studies of synchronization phenomena and the applied aspects of developing microwave generators with controlled characteristics (frequency, output power, phase) of the output radiation. In [1–3], nonautonomous phenomena in certain reference distributed models of microwave electronics and nonlinear oscillation theory and wave theory were analyzed. We imply an electron beam carrying a supercritical electric current or an electron beam with a backward (counterpropagating) wave in cyclotron-resonance conditions [3]. Presently, such a system (a laser based on the cyclotron resonance with a counterpropagating wave) is being intensely investigated as a promising easily adjustable powerful radiation source in the millimeter and submillimeter wavelength ranges [4].

In the present paper, we analyze the transient period of a synchronization regime (i.e., the duration of the transient process) in a distributed system as a function of the phase of an external synchronizing signal. The feasibility of the ultra-fast synchronization of self-oscillations, which proceeds at the optimal phase of an external electromagnetic field, is also shown.

In order to analyze processes occurring in a helical electron beam, we consider a simple self-consistent model [5] described by the equation of motion

$$\frac{d\beta}{d\xi} - j\mu(1 - |\beta|^2)\beta = F \quad (1)$$

and the time-dependent equation for the excitation of a

counterpropagating wave

$$\frac{\partial F}{\partial \tau} - \frac{\partial F}{\partial \xi} = -\frac{1}{2\pi} \int_0^{2\pi} \beta d\theta_0. \quad (2)$$

Here, β is the complex radius of a trajectory for electrons in an ensemble with a phase initially uniformly distributed with respect to the high-frequency electromagnetic field; $F = F(\xi, \tau)$ is the complex dimensionless field amplitude, which slowly varies over the beam cross section; and ξ and τ are the dimensionless longitudinal coordinate and dimensionless time, respectively. The parameter μ is called the nonisochronism parameter, which characterizes the measure of the system's inertia. Equations (1) and (2) are solved with the following initial and boundary conditions:

$$F(\xi, \tau = 0) = f^0(\xi), \quad \beta(\xi = 0) = \exp(j\theta_0), \quad (3)$$
$$\theta_0 \in [0, 2\pi].$$

An external harmonic signal

$$F(\xi = A, \tau) = F_\Omega \exp[j(\Omega\tau + \varphi)]$$

is introduced at the collector end of the system $\xi = A$. Here, A is the extension of the system; F_Ω is the external-signal amplitude; φ is the initial phase of the external electromagnetic field; Ω corresponds to detuning between the external-action frequency and the frequency $\hat{\omega}$ of the cold synchronism, which satisfies the synchronism condition $\hat{\omega} + \beta_0(\hat{\omega})v_{\parallel} = \omega_c$, where $\beta_0(\hat{\omega})$ is the propagation constant of the counterpropagating wave with the frequency $\hat{\omega}$ in a system without an electron beam; and v_{\parallel} is the longitudinal (translational) velocity of the helical flow.

In this consideration, we assume that the external action $F_\Omega \exp[j(\Omega\tau + \varphi)]$ is switched on when the transient process in an autonomous system is completed, and a steady-state generation regime is settled in it. The initial phase φ of the external signal varies from 0 to 2π , whereas the time at which the external action is

Saratov State University,
ul. Astrakhanskaya 83, Saratov, 410026 Russia
e-mail: alkor@cas.ssu.runnet.ru; true@cas.ssu.runnet.ru;
aeh@cas.ssu.runnet.ru

switched on remains fixed. Thus, in fact, the question being analyzed is the magnitude of the effect of the initial phase difference between the steady-state generation regime and the external action on the duration of the time interval in which system synchronization is realized.

In Fig. 1a, the duration of the transient period T is shown as a function of the initial phase φ of the original electromagnetic field, which is characteristic of the external synchronizing signal in different cross sections ξ of the lamp interaction space. The following governing parameters of model (1)–(3) are chosen: $A = 3.0$, $\mu = 2.0$, $\frac{F_\Omega}{F_0} = 0.1$, and $\frac{\Omega}{\omega_0} = 0.0154$; here, F_0 and ω_0 are the amplitude and frequency of the autonomous oscillations, respectively.

As follows from Fig. 1a, the duration of the transient process strongly depends on the initial phase of the input signal and has a clearly pronounced maximum and minimum, the maximal and minimal settling times for the synchronization regime differing by approximately an order of magnitude. The minimal duration of the transient process is $T_{\min} < 20$, which corresponds to only 2–3 characteristic times τ_A of retardation of the distributed feedback for the generator under study. The characteristic time for the system reaction to an external action is determined by the lamp length A , the group velocity v_g of the wave propagation in a waveguide structure, and the beam translational velocity v_{\parallel} . The external field applied to the lamp input propagates in the opposite direction to the beam and performs the modulation of the helical electron flow. This flow, in turn, transfers this information to the lamp input (collector end) with a velocity v_{\parallel} exciting a counterpropagating electromagnetic wave in the waveguide. The field of this wave sums with the external field. As a result, the characteristic time turns out to be equal to $\tau_A \approx A \left(\frac{1}{v_g} + \frac{1}{v_{\parallel}} \right)$, which attains (in terms of dimensionless variables) the value $\tau_A \approx 6.0$.

This fact implies that, in the case of the optimal phase of the external electromagnetic field, the ultrafast synchronization of a distributed self-oscillatory system does occur with a counterpropagating wave, which realizes the feedback. For maximal duration of T , the synchronization regime settles in times $T > 20\tau_A$.

Comparing the dependences $T(\xi)$ for the duration of the transient process, which are plotted for different cross sections of the lamp interaction space (see Fig. 1a), we can see that in the ultrafast synchronization regime a virtually simultaneous settling of a synchronous regime in the entire bulk of the active medium is observed. For an external-field phase φ different from the maximal one, the duration of the transient process differs for different lamp cross sections. The most rapid transient process occurs in the middle of the lamp interaction space: $\xi = \frac{A}{2}$.

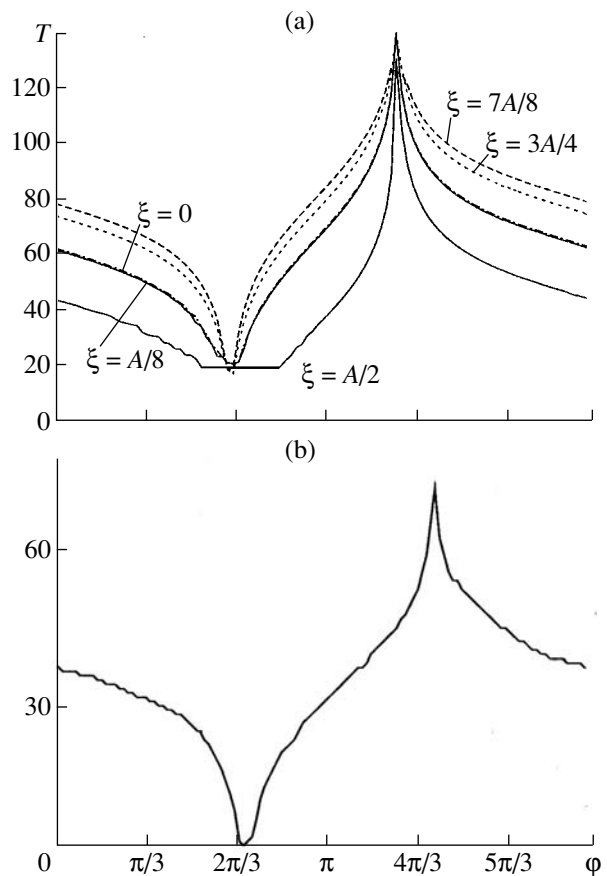


Fig. 1. Duration of the synchronization regime settling: (a) in an active distributed medium represented by a helical flow and counterpropagating electromagnetic wave as a function of the external-field phase. The curves are plotted for different cross sections of the lamp interaction space, and (b) in a Van der Pol generator (the nonlinearity parameter is $\epsilon = 0.1$).

For a qualitative analysis of the phenomenon of self-oscillation ultrafast synchronization in an active distributed medium, we can use the equation of phase synchronization, which was first derived by Adler in [6]. This is the equation to which the analysis of the synchronization phenomenon in different systems is reduced:

$$\dot{\alpha} + \kappa \sin \alpha - (\omega_0 - \Omega) = 0. \quad (4)$$

Here, α is the phase difference between the external signal and the signal of the nonautonomous oscillatory system and κ is the synchronization coefficient, whose shape is determined by the features of the system under study. As is shown in [7], under certain assumptions, synchronization in a helical beam interacting with a counterpropagating wave is described by Eq. (4), the synchronization coefficient being determined by features of electromagnetic-field distributions in a distributed oscillatory system, and depends on the ξ coordinate of the interaction space.

It is worth noting that the same equation describes synchronization by a weak external signal of self-oscil-

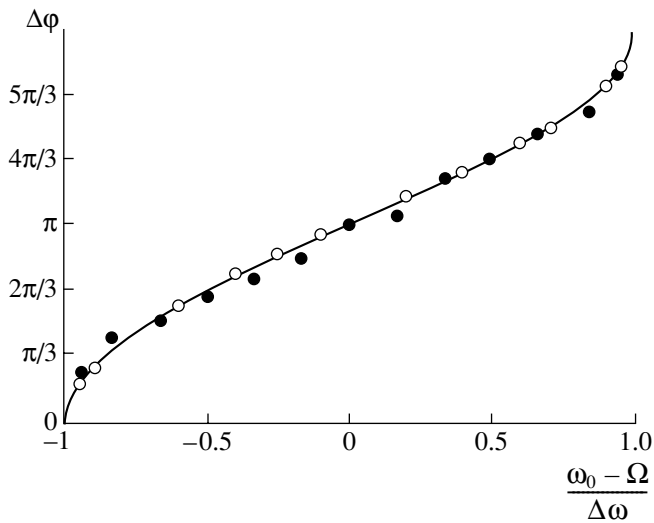


Fig. 2. Phase difference for the maximal and minimal settling time of a transient process as a function of the relative detuning $\frac{\omega_0 - \Omega}{\Delta\omega}$.

lations in a generator described by the Van der Pol equation [8] under the assumption that an external signal changes only the phase of the oscillations but not their amplitude. In the latter case, under a number of simplifying assumptions, $\kappa = \frac{A}{2}$, where A is the amplitude of the external action [8, 9].

The duration T_α of synchronization mode settling in the Van der Pol generator depends on the initial phase φ of the external signal and is presented in Fig. 1b. This duration is determined from Eq. (4) by the condition $|\omega_0 - \Omega| \leq \kappa$. One time unit in Fig. 1b corresponds to one period of system oscillations. Comparing Figs. 1a and 1b, we may conclude that the duration of the transient process as a function of the initial phase φ of the governing electromagnetic field for both the self-oscillatory system and a distributed electron generator has a qualitatively similar shape. In this case, in the Van der Pol generator, an ultrafast synchronization of self-oscillations during one characteristic period can also be obtained by selecting the optimal initial phase of the external field. Using Eq. (4), it is easy to show that the quantity $\Delta\varphi$, which determines the difference of phases corresponding to the maximal and minimal settling time of the transient process as a function of the frequency of an external action in the synchronization region with the width $2\Delta\omega$, can be written out in the analytical form

$$\Delta\varphi = 2\arcsin\frac{\omega_0 - \Omega}{\Delta\omega} + \pi. \quad (5)$$

It follows that the quantity $\Delta\varphi$ is determined only by the frequency detuning $(\omega_0 - \Omega)$.

We now analyze the corresponding expressions

$$\Delta\varphi\left(\frac{\omega_0 - \Omega}{\Delta\omega}\right)$$

for both the distributed self-oscillatory system under investigation and the Van der Pol generator using numerical simulation. In order to find these dependences, we calculated the periods of synchronization mode settling $T(\varphi)$ for different frequencies of an external action at other parameters mentioned above. In Fig. 2, the calculated results for the quantity $\Delta\varphi$ are given in the case of a distributed self-oscillatory system (●) and for the Van der Pol generator (○). In the same figure, the solid line calculated by formula (5) is also presented.

It follows from Fig. 2 that the optimal phase relationships for attaining a minimal time of synchronous mode settling in a complicated electron self-oscillatory medium are described by the same universal equations obtained for a simple finite-dimensional system (Van der Pol generator).

Apparently, we may expect that a similar behavior of the duration of transient processes when settling synchronization regimes is universal for a broad class of linear self-oscillatory systems with both a concentrated and a distributed nature. In this case, the nonautonomous dynamics of these systems can be approximately described by the synchronization equation in the form (4). Here, the most important fact is the possibility of ultrafast settling the synchronization regime. This settling is observed for optimal phase relations between an external governing signal and oscillations in the system.

ACKNOWLEDGMENTS

This work was supported by the Russian Foundation for basic research, project nos. 01-02-17392 and 00-15-96673.

REFERENCES

1. B. E. Zhelezovskii and E. V. Kal'yanov, *Multifrequency Operating Modes in Microwave Devices* (Svyaz', Moscow, 1978).
2. A. E. Khrarov, Radiotekh. Elektron. (Moscow) **44**, 211 (1999).
3. D. I. Trubetskov and A. E. Khrarov, Pis'ma Zh. Tekh. Fiz. **28** (18), 34 (2002).
4. K. L. Felch, B. G. Danly, H. R. Jory, *et al.*, Proc. IEEE **87** (5), 752 (1999).
5. A. Yu. Dmitriev, D. I. Trubetskov, and A. P. Chetverikov, Izv. Vyssh. Uchebn. Zaved., Radiofiz. **34** (9), 595 (1991).
6. R. Adler, Proc. IRE **34** (6), 351 (1949).
7. D. I. Trubetskov and A. E. Khrarov, Izv. Akad. Nauk, Ser. Fiz. **66** (12), 1761 (2002).
8. M. I. Rabinovich and D. I. Trubetskov, *Introduction to the Theory of Oscillations and Waves* (Nauka, Moscow, 1992).
9. V. S. Anishchenko and T. E. Vadivasova, Radiotekh. Elektron. (Moscow) **47**, 133 (2002).

Translated by G. Merzon

On a Cohesion Zone near a Crack Tip under Brittle Fracture

R. V. Gol'dshtein* and G. A. Shatalov**

Presented by Academician A. Yu. Ishlinskiĭ October 28, 2002

Received December 16, 2002

The growth of a crack is accompanied by prefracture processes near its tip, where structural elements are nonlinearly deformed, attain some maximum strain, and fail. The cracking strength of the material is determined by processes in the tip region. Beginning with [1, 2], many authors used crack models (see, e.g., [3, 4] and references therein) in which the tip region of a crack and various forces (cohesion forces) between its edges were considered. The magnitude of such forces generally depends on the crack opening and on the properties of various structural bonds in the material under consideration. The tip-to-crack size ratio is important for modeling the cracking strength and the conditions of both the ultimate equilibrium and crack growth. Indeed, the tip region formed under brittle fracture is much smaller than the crack, while the tip region formed under plastic fracture can be comparable with the crack. In order to understand the features of the cracking strength of materials, it is important to estimate the sizes of the tip region of the crack with specific models for bonds (interactions) between the crack edges and particular mechanisms of deformation and breakage of these bonds.

In this work, we estimate the size of the tip region in an atomistic (lattice) model of a crack. The breakage of an interatomic bond is treated as an elementary act of fracture.

We consider the one-dimensional atomistic model of an opening mode crack (Fig. 1). Atoms interacting pairwise are in the two semi-infinite (upper and lower) chains. This interaction is nonlinear and is described in

the bilinear approximation

$$f_j = \begin{cases} \beta y_j, & y_j \leq u_0 \\ -\frac{\beta}{\eta - 1}(y_j - \eta u_0), & u_0 \leq y_j \leq \eta u_0 \\ 0, & y_j \geq \eta u_0. \end{cases} \quad \begin{matrix} \text{(III)} \\ \text{(II)} \\ \text{(I)} \end{matrix} \quad (1)$$

Here, f_j is the interaction force; y_j is the displacement of the j th atom; β is the stiffness of springs imitating cohesion forces; and η and u_0 are the parameters. Figure 2 shows function (1).

Interaction between atoms in one chain is simulated by semicircular springs with bending stiffness γ . External transverse forces P are applied to the chain ends.

Regions (I), (II), and (III) in Figs. 1 and 2 are the open crack zone, where cohesion forces are absent; the tip region (cohesion zone) described by the descending straight line in Fig. 2; and the elastic-deformation region, respectively.

The model presented in Fig. 1 was discussed in [5–8], where, however, only one or no interatomic bond was introduced in cohesion zone (II).

In order to analyze the cohesion-zone length and fracture process, it is necessary to find displacements $y_j(\text{I})$ ($j = 0, 1, \dots, m - 1$), $y_j(\text{II})$ ($j = 0, 1, \dots, s - 1$), and $y_j(\text{III})$ ($j = 0, 1, \dots$) in the three zones, where m and s are

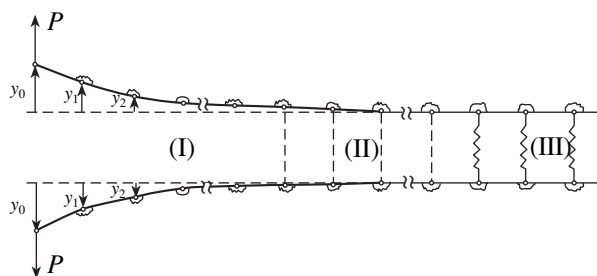


Fig. 1. One-dimensional model of an opening mode crack with the cohesion zone.

* Institute for Problems in Mechanics,
Russian Academy of Sciences, pr. Vernadskogo 101,
Moscow, 117526 Russia

** MATI—Tsiolkovsky Russian State Technological
University, Orshanskaya ul. 3,
Moscow, 121552 Russia

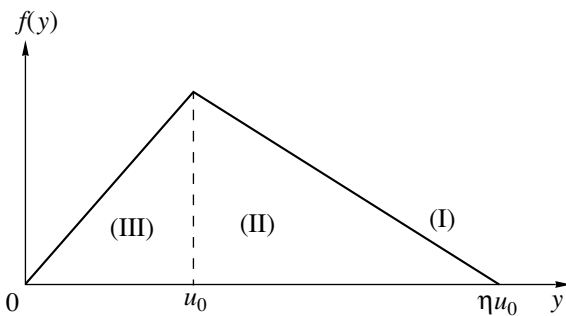


Fig. 2. Interatomic interaction force in a material with a crack.

the lengths of the open crack zone and cohesion zone, respectively. These displacements are the solutions to the equations

$$\frac{\partial w}{\partial y_j} = 0, \quad (2)$$

where

$$w = -2Py_0 + \gamma \sum_{j=1}^{\infty} (y_{j-1} - 2y_j + y_{j+1})^2 + 2\beta \sum_{j=m+s}^{\infty} y_j^2 + 2\beta \sum_{j=m}^{m+s-1} (y_j - u_0) \left[u_0 - \frac{\beta}{\eta - 1} (y_j - \eta u_0) \right] \quad (3)$$

is the deformation energy of the crack. Equation (3) does not contain the surface energy, because this energy is independent of y_j and does not enter into the equations for y_j by virtue of Eq. (2).

Specific finite-difference equations for each zone shown in Fig. 1 follow from Eqs. (2) and (3), and their solutions are sought in the form

$$y_j = C\lambda^j, \quad (4)$$

where C is a constant. We find the following solutions in the three regions:

$$y_j(\text{I}) = \frac{P}{6\gamma}(j^3 - j) + (y_1 - y_0)j + y_0, \quad (5a)$$

$$y_j(\text{II}) = C_1\lambda_1^j + C_2\lambda_2^j + C_3\lambda_3^j + C_4\lambda_4^j + \eta u_0, \quad (5b)$$

$$\lambda_{1,2} = 1 + \rho\alpha \pm (\rho^2\alpha^2 + 2\rho\alpha)^{1/2},$$

$$\lambda_{3,4} = 1 - \rho\alpha \pm (\rho^2\alpha^2 - 2\rho\alpha)^{1/2},$$

$$\alpha = \frac{1}{2}\sqrt{\frac{2\beta}{\gamma}}, \quad \rho = (\eta - 1)^{-1/2},$$

$$y_j(\text{III}) = 2r^j(A\cos j\varphi + B\sin j\varphi), \quad (5c)$$

$$\alpha = \frac{\sin^2\varphi}{\cos\varphi}, \quad r = \frac{1 - \sin\varphi}{\cos\varphi}, \quad 0 \leq \varphi \leq \frac{\pi}{2}.$$

The constants y_0 , y_1 , C_1 , C_2 , C_3 , C_4 , A , and B are found from the matching conditions at the (I)–(II) and (II)–(III) boundaries. It is easy to determine these constants, but the corresponding expressions are very cumbersome and are not presented here.

Using Eqs. (5), we simulated fracture processes numerically. In this case, we follow Novozhilov [9] and treat a crack as a certain “nontrivial form of equilibrium elastic deformation” occurring in an elastic body under the action of external tensile loads.

The basic idea of our simulation is as follows. We assume that each displacement $y_0(\text{I})$ of the edge atom that is subjected to an external force P corresponds to the unique equilibrium state of a body with a crack. The state is characterized by the displacements $y_j(\text{I})$, $y_j(\text{II})$, and $y_j(\text{III})$, crack length m , cohesion-zone length s , and external force P . During simulation, we used the dimensionless quantities $y_j \equiv \frac{y_j}{u_0}$ and $P \equiv \frac{P}{2\rho\alpha\gamma u_0}$. As $y_0(\text{I})$

increases monotonically, equilibrium states replace each other. Thus, fracture is treated as a quasistatic process.

The initial state of the simulation is taken as a perfect crystal, i.e., $m = 0$ and $s = 0$. Specifying the basic parameters $\frac{\beta}{\gamma}$ and η , we calculate the parameters and constants entering into Eqs. (5). Since the condition $y_0(\text{I}) < 1$ corresponds to an elastically deformed crystal with no cracks, we then set $y_0(\text{I}) = 1$ and find the load P . This is the value at which the transition to a new state with $m = 0$ and $s = 1$ occurs.

Then, we increase $y_0(\text{I})$ and find a new P value. This value is used to determine $y_j(\text{II})$ and $y_j(\text{III})$ from Eqs. (5b) and (5c). If $y_0(\text{II}) > \eta$ for an atom in region (II), the atom is treated as being in region (I). In this case, the crack length increases by $\Delta m = 1$ and the cohesion-zone length decreases by $\Delta s = 1$. Similarly, if $y_0(\text{III}) > 1$ for an atom in region (III), the atom is treated as being in region (II). In this case, the cohesion-zone length increases by $\Delta s = 1$, and so on. The simulation provides a dependence of $P = P(m)$.

This dependence is shown in Fig. 3 for $\frac{\beta}{\gamma} = 0.1$ and $\eta = 2$. We also considered some other cases $\left(\frac{\beta}{\gamma} = 1, 0.01 \text{ and } \eta = 2, 3\right)$. The curve in Fig. 3 is typical for all these cases.

The dependence shown in Fig. 3 is similar to a “dinosaur’s back” (this term was introduced in [7]). This dependence testifies to the lattice trapping effect [5, 6, 8, 9]. As is seen in Fig. 3, both growth and healing of a crack beginning with a certain crack length m are accompanied by an increase in the external load P or, in

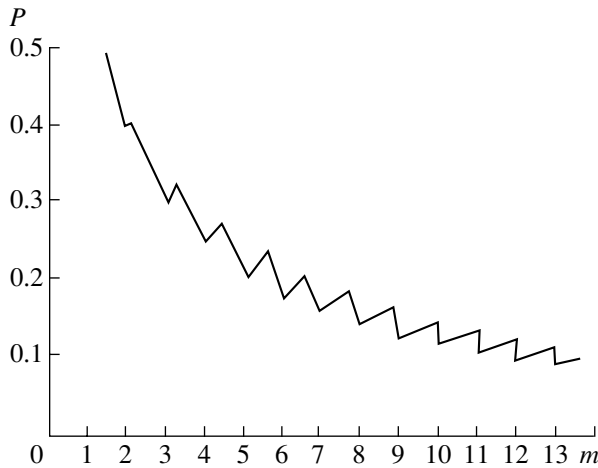


Fig. 3. Equilibrium load as a function of the crack length.

other words, involve passage through a potential barrier (this is the essence of the lattice trapping effect).

We determined that the cohesion-zone length is $s = 0$ and 1 at the ascending and descending branches of the $P(m)$ dependence, respectively. We found no more s values. For $\frac{\beta}{\gamma} = 0.1$ and $\eta = 3$, we found that $s = 1$ and $s = 2$ at these branches, respectively. Other variants considered belong to one of the two cases. Thus, the cohesion zone (tip region) is very short in the atomistic crack model under consideration.

Our study shows that only two regimes of crack growth are possible. If a crack is short ($m \leq 9$ for the case shown in Fig. 3), an interatomic bond being elastic

in region (III) is torn slightly when $y_0(\text{III}) > 1$, and the two interacting atoms are in cohesion zone (II). Finally, when $y_0(\text{II}) > \eta$, the interatomic bond breaks down, and the two atoms are located at the different crack edges in open crack zone (I). The fracture regime changes for $m \geq 10$. When displacement $y_0(\text{III})$ becomes equal to $y_0(\text{III}) = 1$, a pair of interacting atoms passes to zone (I), escaping zone (II). The vertical sections in the dependence $P = P(m)$ shown in Fig. 3 correspond to such jump transitions. The same change in the fracture regime was also observed in other variants considered (but the critical m values were different).

REFERENCES

1. G. I. Barenblatt, Prikl. Mat. Mekh. **23** (3), 434 (1959); Prikl. Mat. Mekh. **23** (4), 706 (1959); Prikl. Mat. Mekh. **23** (5), 893 (1959).
2. D. S. Dugdale, J. Mech. Phys. Solids **8** (2), 100 (1960).
3. B. N. Cox and D. B. Marshall, Acta Metall. Mater. **42** (3), 341 (1994).
4. R. Goldstein and M. Perelmuter, Int. J. Fract. **99** (1/2), 53 (1999).
5. R. Thomson, C. Hsieh, and V. Rana, J. Appl. Phys. **42** (8), 3154 (1971).
6. E. R. Fuller and R. M. Thomson, Fract. Mech. Ceram. **4**, 507 (1978).
7. R. M. Thomson, in *Mechanics. News in Foreign Science. Atomistics of Fracture* (Mir, Moscow, 1987), pp. 107–114.
8. N. F. Morozov and M. V. Paukshto, *Discrete and Hybrid Models of Fracture Mechanics* (S.-Peterburg. Gos. Univ., St. Petersburg, 1995).
9. V. V. Novozhilov, Prikl. Mat. Mekh. **33** (5), 797 (1969).

Translated by V. Chechin

TECHNICAL
PHYSICS

Shock Wave Processes and Cumulation in a Steel Ball under Quasi-Spherical Explosive Loading with Perturbation

A. É. Kheifets¹, N. P. Purygin², N. Yu. Frolova¹, V. I. Zel'dovich^{1,*},
Academician B. V. Litvinov², and V. I. Buzanov²

Received September 6, 2002

The spherical cumulation of shock waves in solids makes it possible to investigate the properties of a substance at ultrahigh pressures. However, the exact spherical symmetry of a shock wave in a substance under study is not a necessary condition of spherical cumulation. The same pressures as at exact spherical detonation can be achieved with low-symmetry (quasi-spherical) explosive generators if the shock wave generated in the sample material becomes spherically symmetric at a certain stage of the shock wave process, i.e., if motion becomes self-similar. It was established in [1] that the dodecahedral shock wave loading of metallic samples can provide a centrosymmetric converging shock wave, where pressure increases according to the laws of spherical cumulation.

Investigation of noncentrosymmetric loading schemes includes the important problem of the stability of generated cumulation under varying initial experimental conditions. The general approach is as follows. Investigation of the behavior of model metals and alloys with the well-studied spectrum of phase transformations under nonspherical shock wave loading reveals the evolution features of a complex shock wave front. The loaded material “fixes” the external action, which makes it possible to reproduce the pattern of shock wave motion. The perturbation of the detonation wave (i.e., of the initial experimental conditions) gives rise to the spatial separation of interaction traces corresponding to different loading stages. As the shock wave moves towards the cumulation point, the initial conditions of the experiment are forgotten, and the symmetry of the wave increases. Correspondingly, the geometry of traces changes. In this work, the mechanism of the two-stage concentration of tensile stresses at the focus-

ing center, which is responsible for the formation of a cavity at the cumulation point, is revealed and studied in this approach.

Solid steel ball samples 40 mm in diameter were subjected to the action of a quasi-spherical shock wave with increasing pressure near the focusing center up to 200 GPa or more [1, 2]. Samples were covered with a 20-mm-thick explosive-material layer and placed in a massive metallic shell preventing the fracture of the ball [3]. The charge surface was equipped with 12 detonators, which enables us to simultaneously detonate the explosive material at 12 points with an asynchronism of no more than 0.1 μ s.

The aim of the work is to study the possibility of cumulating energy when the symmetry of the loading scheme is broken. The symmetry was broken by turning off one of the detonators; as a result, a quasispherical perturbed converging shock wave was generated in a sample. The sample that was studied in detail in [1, 2] was taken as an etalon. This sample was loaded by using all 12 initiation points, i.e., without breaking the dodecahedral symmetry of the experiment.

It was shown in [1, 2] that dodecahedral unperturbed explosive loading gave rise to the formation of a single quasispherical shock wave front at distance $r_0 \approx 9$ mm from the focusing center, and pressure for $r < r_0$ increases according to the laws of spherical cumulation.

Figure 1 shows the diameter section of the etalon sample after chemical etching. At a distance of half the radius in the outer part of the ball, there are figures in the form of arcs with the centers near the projections of the initiation points, i.e., Altshuler figures (indicated by the arrow). Arcs were interpreted as interfaces of the boundaries of the contact discontinuity of Mach configurations arising when shock waves moving from the neighboring initiation points interact with each other [2]. In the process of motion, Mach waves smoothed the complex front of shock waves propagating from 12 initiation points, and the front became spherically symmetric. In the inner part of the ball, the shock wave motion is one-dimensional beginning at half the radius.

At the center of the ball, a spherical cavity arose, and two ring zones were formed around it. Investigation

¹ Institute of Metal Physics, Ural Division,
Russian Academy of Sciences,
ul. S. Kovalevskoi 18, Yekaterinburg, 620219 Russia

² Russian Federal Nuclear Center All-Russia Research
Institute of Technical Physics,
Snezhinsk, Chelyabinsk oblast, 454070 Russia

* e-mail: zeldovich@imp.uran.ru

of microstructure and microhardness indicated that melting with further crystallization and hardening to bainite occurred in the inner zone. In the second (outer) zone, austenite was formed with further hardening to bainite. Thus, the remaining (after unloading) temperatures at the outer boundaries of zones were equal to the melting point of steel and austenite formation temperature, i.e., to about 1500 and 800°C, respectively. Pressure at the outer boundaries of ring zones was equal to 200 and 140 GPa, respectively. The pressure at the inner boundaries of the zones was significantly larger.

The alternation of zones of the changed microstructure around the central cavity indicates that pressure increases as shock waves move towards the focusing center; i.e., cumulation occurs. The absence of traces of the original symmetry in the configuration of zones testifies to the “forgetting” of the initial conditions.

Figure 2 shows the diameter section of the sample for the experiment with a broken symmetry. The missed initiation point lies in the section plane. The disturbed sample, as well as the etalon one, includes Altshuler figures, a central cavity, melting zone, and bainite-transformation zone. The average sizes of these zones virtually coincide with the corresponding sizes of the etalon sample (the cavity in the broken-symmetry sample is somewhat smaller). Comparison between samples (Figs. 1, 2) testifies to the presence of cumulation under perturbation. Differences that enable one to reveal the features of shock wave motion with a broken symmetry are of primary interest.

The experiment with perturbation has the following features.

(1) There is a narrow section of a changed microstructure state, which has the shape of an elongated triangle, whose acute angle is directed to the missed initiation point.

(2) The geometric centers of zones with changed microstructure are regularly shifted towards the same side. On the contrary, a noticeable shift of the central cavity with respect to the geometric center of the sample is absent. Figure 3 shows the microstructure of the central part of the broken-symmetry sample. The zone of melting and further crystallization with the dendrite structure is located around the central cavity. The arrows indicate the boundary of this zone. The shift of the melting zone with respect to the cavity is pronounced.

The presence of the triangle section of the changed microstructure state (Figs. 2, 4) indicates that pressure and temperature increase locally near the line joining the focusing center and missed initiation point. A change in the microstructure in this region is associated with interaction between waves moving from five initiation points neighboring to the missed point. Two such waves are schematically shown by arcs in Fig. 2. Waves form a pyramid whose base is a regular pentagon and whose vertex is directed to the missed initiation point. Interacting waves, the lateral faces of the pyramid,

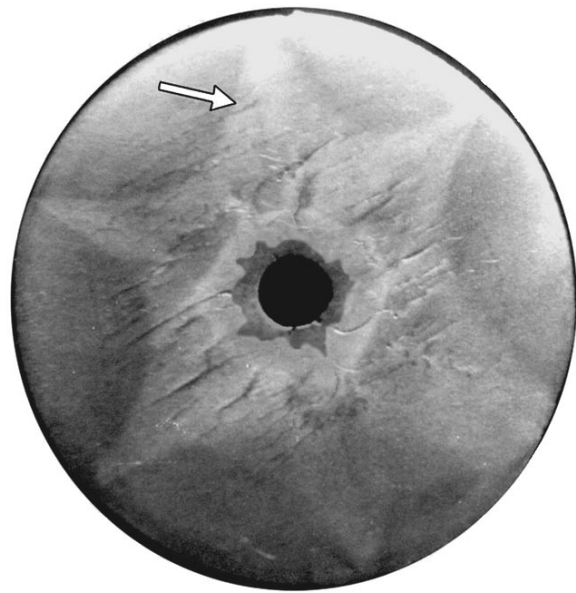


Fig. 1. Diameter section of the sample loaded with 12 initiation points (etalon experiment). The arrow points to Altshuler figures.

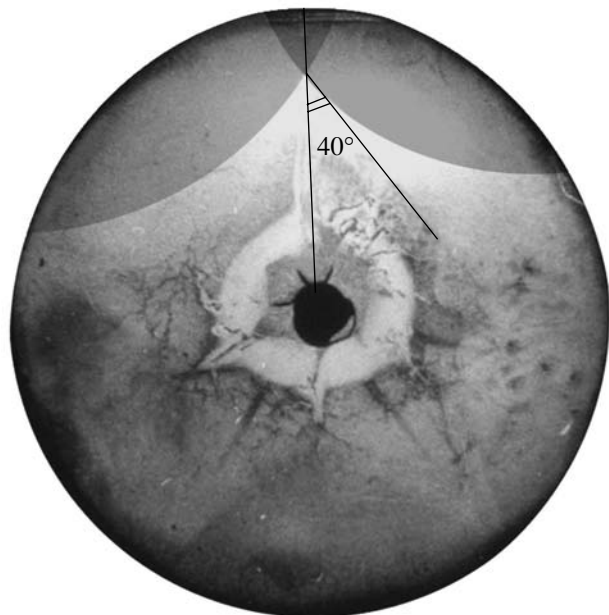


Fig. 2. Diameter section of the sample in the experiment with perturbation. The arcs are the moving waves, lateral faces of the pyramid, forming the Mach configuration.

move towards the center of the ball, and the pyramid thus decreases gradually in size. Since interacting waves are not plane waves (Huygens construction provides quite a complex surface), as the pyramid decreases in size, the angle α between the lateral face and height increases and reaches the critical value α_{cr} at

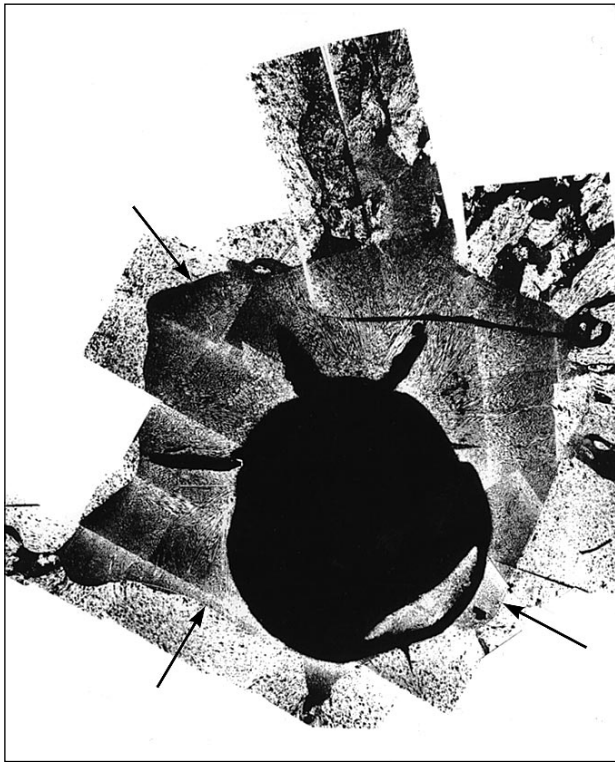


Fig. 3. Microstructure of the central part of the diameter section of the sample in the experiment with perturbation. The arrows indicate the boundary of the melting zone.

a certain instant (Fig. 2). Then, a Mach shock wave and associated narrow cumulative jet arise at the vertex of the pyramid. Thus, the triangle region is the trace of the motion of the Mach wave and has the same nature as the Altshuler figures observed in the experiments reported in [2]. The difference between the intensities of the observed effects in the cases of the narrow triangle and the Altshuler figures can be attributed to the fact that the analogue of the angle α in the latter case exceeds the critical value α_{cr} . The Mach configuration is substantially more unsteady; therefore, the local increase in pressure and remaining temperature is significantly smaller.

The Mach wave trace that was observed in the experiment with perturbation enables one to directly extract the angle α_{cr} from the experiment by making Huygens constructions for the five-wave configuration of the pyramid shape described above. The vertex of the pyramid coincides with the vertex of the triangle region corresponding to the point of originating the Mach wave (Fig. 2). The α_{cr} value obtained by this method is equal to about 40° . Since the above five-wave scheme differs only slightly from the classical cumulative crater (a cone is considered in the classical scheme instead of the pyramid), it can be assumed that this α_{cr} value remains for the conic cumulation of shock waves in steel.

The shift of the ring zones of the changed microstructure with respect to the geometric center of the sample indicates that the presence of perturbation leads to the change in the position of the cumulation point. Pressure reaches its maximum value near the melting zone, i.e., at a distance of several millimeters from the ball center. The noncoincidence of the central cavity with the cumulation center means that the cavity is formed primarily through processes that are not directly associated with energy cumulation.

The cavity shape is disturbed in the experiment with perturbation. As follows from Figs. 2 and 3, the cavity is doubled, i.e., consists of two mutually penetrating spheres of different radii. The center of the larger sphere coincides with the geometric center of the ball, and the center of the smaller sphere is located near the focusing point of shock waves, which does not coincide with the geometric center of the sample. Analyzing the causes of the observed distortion of the cavity shape, we can propose the hypothesis of the two-stage formation of the cavity and describe mechanisms responsible for each stage.

The formation of the cavity is associated with the concentration of omnidirectional tensile stresses at a certain point of the sample. These stresses are caused by the action of rarefaction waves and unloading. It is known that an unloading wave overtakes a compression shock wave moving from the sample surface. The geometry of the unloading wave coincides with the geometry of the compression wave. Therefore, both waves focus at the same point. After the shock wave that is reflected from the focusing center reaches the free surface, a rarefaction wave accompanied by the doubling of the mass velocity again moves to the center of the ball [4]. At the instant of focusing of this wave, the initial conditions of the experiment can be completely forgotten, and the concentration of tensile stresses reaches a maximum near the geometric center of the ball. If stresses exceed the ultimate strength, a discontinuity arises in the sample. The basic part of the cavity in the experiment with perturbation is formed in just such a way; otherwise, its position at the center of the ball could not be explained. At the same time, the forgetting of the initial conditions implies the appearance of a cavity of regular spherical shape. The presence of distortion indicates that a certain discontinuity exists in the sample at the instant of focusing of the rarefaction wave reflected from the ball surface.

Let us reconstruct the shape of the central part of the sample at the instant of the formation of the spherical cavity at the ball center. To this end, a sphere of radius R_0 (light circle in the left part of Fig. 4) at the center is taken so that it most closely touches the boundaries of the cavity, and we use the mass conservation law

$$\frac{4}{3}\pi r'^3 = \frac{4}{3}\pi r^3 - \frac{4}{3}\pi R_0^3,$$

where r' and r are the radius vectors of an arbitrary

point of the sample before and after cavity formation, respectively. Using a computer program, one can process the photograph of the sample according to the above formula and obtain the image of the diameter section of the ball before the formation of the cavity covered by the R_0 sphere.

The right panel of Fig. 4 shows the sample pattern reconstructed by the above computer method. It is seen that a discontinuity of the almost regular spherical shape, which excludes accidental circumstances and corroborates the above arguments, really exists at the focusing point of shock waves (melting-zone center).

One can conclude that the cavity is formed in two stages. First, a discontinuity is formed at the focusing center of the shock wave. This effect can be attributed to the fact that the pulse duration in experiments is limited, and a rarefaction wave (pressure decrease at the pulse tail) overtakes the shock wave. For an ideal shock wave, with an infinite step at the cumulation center, the only point with zero density is formed [5]. In the real experiment, with a finite step, a rapid decrease in pressure at the pulse tail increases the outflow of a substance from the cumulation center, and the point transforms to a macroscopic cavity. The shock wave is then reflected from the focusing center and moves to the sample surface. After the shock wave arrives at the free surface, a new rarefaction wave moves to the ball center and gives rise to the formation of the second, larger, discontinuity (as follows from Fig. 4). In symmetric experiments, both cavities merge into one, because the focusing center coincides with the geometric center of the sample.

Thus, investigation of the features of quasi-spherical cumulation with perturbation provides the following conclusions. The breaking of the experimental symmetry by missing one of the initiation points gives rise to a shift of the focusing center with respect to the unperturbed position. The initial conditions are forgotten in the process of motion of the shock wave front, and the shock wave becomes more symmetric. The increase in the symmetry of the shock wave front in the process of motion enables one to follow the sequence of specific shock wave phenomena in the sample material (origin of Mach configurations, local changes in the microstructure, and discontinuities). The presence of two

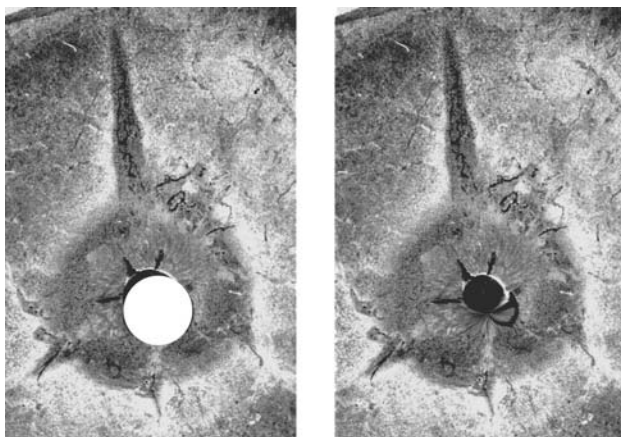


Fig. 4. Two stages of the formation of the central cavity: (left panel) separation of the spherical cavity arising at the second stage and (right panel) computer reconstruction of the first stage.

stages in the formation of the central cavity is revealed by this method.

It was established that the cumulation implemented in the experiments is stable under small perturbations in the initial conditions, and this does not contradict the instability of unlimited cumulation investigated by Academician Zababakhin [5].

REFERENCES

1. V. I. Zel'dovich, B. V. Litvinov, N. P. Purygin, *et al.*, Dokl. Akad. Nauk **343**, 621 (1995) [Phys. Dokl. **40**, 401 (1995)].
2. A. É. Kheifets, N. Yu. Frolova, V. I. Zel'dovich, *et al.*, Izv. Ross. Akad. Nauk, Ser. Fiz. **62** (7), 1303 (1998).
3. V. I. Buzanov and N. P. Purygin, in *Detonation. Proceedings of X Symposium on Detonation and Explosion, Chernogolovka, 1992*, p. 131.
4. Ya. B. Zel'dovich and Yu. P. Raizer, *Elements of Gas Dynamics and the Classical Theory of Shock Waves* (Fizmatgiz, Moscow, 1963; Academic, New York, 1968).
5. E. I. Zababakhin and I. E. Zababakhin, *Phenomena of Unlimited Cumulation* (Nauka, Moscow, 1988).

Translated by R. Tyapaev

TECHNICAL
PHYSICS

Effect of Microdefects on the Adhesion-Separation Work for Joint Materials

R. V. Gol'dshtein* and M. E. Sarychev**

Presented by Academician A. Yu. Ishlinskiĭ October 3, 2002

Received October 10, 2002

Practical applications require physical models for estimating the adhesion characteristics of interfaces between joint materials and the effect of crystal-structure defects in these materials on those characteristics [1]. In [2–4], a thermodynamic model using the Gibbs equation was proposed for estimating the variation in the surface tension of interfaces with the content of vacancies, dislocations, and impurities.

In this study, we developed a general model describing the effect of lattice defects on an important characteristic of the interlayer-connection strength, namely, the work w_1 of separation of two adjacent (crystalline) materials. The case where such defects are vacancies is analyzed in detail. It turns out that, as the concentration of vacancies increases, w_1 passes through a maximum (minimum) or decreases monotonically depending on the physical conditions and properties of materials. Generating a sufficient concentration of vacancies in one of the materials, it is possible to make w_1 vanish or even negative, which must result in the spontaneous separation of materials. These theoretical results for the strength properties of interfaces are important for designing new (in particular, layered) materials with an increased fracture strength and for estimating the durability of the joints under the action of mechanical loads and physicochemical fields.

We consider a plane interface between two crystalline materials 1 and 2 with structural defects of types 1 and 2, respectively. Similar to [2–4] (see also [5]), we consider the interface as a surface that can adsorb (desorb) defects from the bulk.

Let these materials be subjected to a mechanical stress σ that is perpendicular to the interface and gradually increases the gap between them up to their complete separation. This stress $\sigma = \sigma(\delta)$ is a certain func-

tion of the displacement δ of the interface walls with respect to their position in the initial (unloaded) state. In this case, the work w_1 (per unit interface area) spent on the separation of materials is equal to

$$w_1 = \int_0^{\delta_c} \sigma(\delta) d\delta, \quad (1)$$

where $\delta = 0$ corresponds to the initial state of the interface and $\delta = \delta_c$ is the minimum displacement at which materials 1 and 2 can already be considered as separated [i.e., $\sigma(\delta_c) = 0$].

The w_1 value must depend on the character of the separation process. In particular, the following limiting cases can be considered (see also [6]).

(i) “Slow” separation, when equilibrium between the interface and materials holds for constant chemical potentials μ_1 and μ_2 of defects in the material bulks; i.e., $\sigma = \sigma(\delta, \mu_1, \mu_2)$ and $w_1 = w_1(\mu_1, \mu_2)$. In this case, to find the work w_1 , we use the equation that is the Legendre transform of the Gibbs equation [5] and relates the differentials $d\mu_1$, $d\mu_2$, and $dw_1 = \sigma d\delta$ (temperature and pressure are considered constant in the system):

$$\sigma d\delta - \Gamma_1 d\mu_1 - \Gamma_2 d\mu_2 = d(\Phi - \mu_1 \Gamma_1 - \mu_2 \Gamma_2), \quad (2)$$

where Γ_1 and Γ_2 are the numbers of defects 1 and 2 at the interface, respectively, and Φ is the Helmholtz free energy of the interface (all quantities are taken per unit interface area). In this case, the relationships $\frac{\partial \sigma}{\partial \mu_i} =$

$-\frac{\partial \Gamma_i}{\partial \delta}$, $i = 1, 2$ follow from Eq. (2). Using them after the differentiation of Eq. (1) with respect to μ_i , we obtain the following system of equations:

$$\frac{\partial w_1}{\partial \mu_i} = \Gamma_{i0}(\mu_1, \mu_2) - \Gamma_{ic}(\mu_i), \quad i = 1, 2, \quad (3)$$

where Γ_{i0} is the number of i th defects per unit interface area for $\delta = 0$ and Γ_{ic} is the Γ_i value for $\delta = \delta_c$, i.e., the number of i th defects per unit free-surface area formed on the i th material after separation. In this case, it is

* *Institute for Problems in Mechanics,
Russian Academy of Sciences,
pr. Vernadskogo 101, Moscow, 117526 Russia*

** *Institute of Physics and Technology,
Russian Academy of Sciences,
ul. Krasikova 25a, Moscow, 117218 Russia*

assumed that the surface of a given material in the separated state contains only its own defects and, therefore, $\Gamma_{ic} = \Gamma_{ic}(\mu_i)$.

(ii) "Fast" separation, when the number Γ_1 and Γ_2 of defects at the interface do not vary but μ_1 and μ_2 do vary. Therefore, $\sigma = \sigma(\delta, \Gamma_1, \Gamma_2)$; i.e., $w_1 = w_1(\Gamma_1, \Gamma_2)$. Immediately using the Gibbs equation [5] $\sigma d\delta + \mu_1 d\Gamma_1 + \mu_2 d\Gamma_2 = d\Phi$, we arrive at the relationship $\frac{\partial \sigma}{\partial \Gamma_i} = \frac{\partial \mu_i}{\partial \delta}$, $i = 1, 2$.

Substituting these relationships into Eq. (1), differentiated with respect to Γ_i , we obtain the following equations for $w_1(\Gamma_1, \Gamma_2)$:

$$\frac{\partial w_1}{\partial \Gamma_i} = \mu_{ic}(\Gamma_i) - \mu_{i0}(\Gamma_1, \Gamma_2), \quad i = 1, 2, \quad (4)$$

where μ_{i0} and μ_{ic} are the μ_i values for $\delta = 0$ and $\delta = \delta_c$, respectively.

Thus, if we express the quantities μ_i , Γ_{i0} , Γ_{ic} , or Γ_i , μ_{i0} , μ_{ic} , in terms of the defect concentrations C_1 and C_2 in the bulks of the adjacent materials in a certain model, set of equations (3) or, correspondingly, (4) makes it possible to find the dependence for the separation work $w_1(C_1, C_2)$.

We obtain and analyze the dependence $w_1(C_1, C_2)$ for the slow-separation mode [Eq. (3)], when the adjacent materials contain nonequilibrium vacancies. The chemical potential of these vacancies is given by the expression [7]

$$\mu_i = kT \ln \frac{C_i}{C_{ie}}, \quad i = 1, 2, \quad (5)$$

where C_{ie} are the equilibrium values of vacancy concentrations C_i , T is the temperature, and k is the Boltzmann constant.

Following [2], we will determine Γ_{i0} as

$$\Gamma_{i0} = \frac{C_{li} b}{\Omega_i}, \quad (6)$$

where $0 \leq C_{li} < 1$ is the concentration of i th-material vacancies in the unloaded interface, Ω_i is the volume of i th-type vacancies, and b is the interface thickness for $\delta = 0$. Further, we use the model according to which the interface can be considered as a surface that can adsorb vacancies [5]. Similar to [2], we also assume that the vacancies are adsorbed from each material independently, while they are desorbed only into the material from which they are adsorbed. In this case, the kinetics of the concentration C_{li} are described by the equation [2]

$$\frac{dC_{li}}{dt} = K_{ai}(1 - C_{li})C_i - K_{di}C_{li}(1 - C_i), \quad (7)$$

where K_{ai} and K_{di} are the constants of adsorption and desorption for vacancies under their exchange between the i th-material bulk and the interface. In the steady mode $\left(\frac{dC_{li}}{dt} = 0\right)$, it follows from Eqs. (6) and (7) that

$$\Gamma_{i0} = \frac{bh_i}{\Omega_i} \frac{C_i}{1 + (h_i - 1)C_i}, \quad h_i = \frac{K_{ai}}{K_{di}}. \quad (8)$$

Similar representations are also used to describe the exchange of vacancies between the bulk of each material and its free surface formed after separation. In this case, we take into account that, since the μ_i values hold in the slow-separation mode, the quantities C_i are also conserved by virtue of Eq. (5). Therefore, we have the following expression, similar to Eq. (8), for Γ_{ic} :

$$\Gamma_{ic} = \frac{d_i h_{ic}}{\Omega_i} \frac{C_i}{1 + (h_{ic} - 1)C_i}, \quad (8')$$

where $h_{ic} = \frac{K_{ai}^{(c)}}{K_{di}^{(c)}}$; $K_{ai}^{(c)}$ and $K_{di}^{(c)}$ are the constants of adsorption and desorption for vacancies on the free surface of the i th material and d_i is the thickness of the surface layer of the i th material in which these processes occur.

Substituting Eqs. (5), (8), and (8') into Eq. (3) and introducing the dimensionless quantity $\bar{w}_1 = w_1 \frac{\sqrt{\Omega_1 \Omega_2}}{bkT}$, we find that

$$\frac{\partial \bar{w}_1}{\partial C_i} = \frac{A_i}{1 + D_i C_i} - \frac{B_i}{1 + E_i C_i}, \quad (9)$$

where

$$A_i = \frac{h_i \sqrt{\Omega_1 \Omega_2}}{\Omega_i}, \quad B_i = \frac{h_{ic} d_i \sqrt{\Omega_1 \Omega_2}}{b \Omega_i},$$

$$D_i = h_i - 1, \quad \text{and} \quad E_i = h_{ic} - 1$$

are the dimensionless parameters. Since the variables C_1 and C_2 are completely separated in Eq. (9), the solution of Eq. (9) has the form

$$\bar{w}_1(C_1, C_2) = \bar{w}_1^{(0)} + \sum_{i=1}^2 \left[\frac{A_i}{D_i} \ln \left(\frac{1 + D_i C_i}{1 + D_i C_{ie}} \right) - \frac{B_i}{E_i} \ln \left(\frac{1 + E_i C_i}{1 + E_i C_{ie}} \right) \right], \quad (10)$$

where $\bar{w}_1^{(0)} \equiv w_1(C_{1e}, C_{2e}) \frac{\sqrt{\Omega_1 \Omega_2}}{bkT}$.

For applications, it is of interest to determine the values of parameters for which the dependence $w_1(C_1, C_2)$ has an extremum (maximum or minimum) and whether it can become negative. The latter property

would indicate adhesion incompatibility of the materials for a certain vacancy content in them.

Since Eq. (9) must be equal to zero at a possible extremum, the values $C_1 = C_1^*$ and $C_2 = C_2^*$ at this point are determined as

$$C_1^* = \frac{B_1 - A_1}{A_1 E_1 - B_1 D_1}, \quad C_2^* = \frac{B_2 - A_2}{A_2 E_2 - B_2 D_2}. \quad (11)$$

We substitute Eq. (9) into Eq. (10). It is easy to show that $0 \leq C_i^* < 1$, only if either

$$h_{ic} > h_i \frac{b}{d_i}, \quad \frac{d_i}{b} < 1 \quad (12a)$$

or

$$h_{ic} < h_i \frac{b}{d_i}, \quad \frac{d_i}{b} > 1. \quad (12b)$$

According to the general theory of functions of two variables, $w_1(C_1, C_2)$ has an extremum at $C_i = C_i^*$ if $\Delta = R_{11}R_{22} - R_{12}^2 > 0$ for these values of C_i , where $R_{ii} = \frac{\partial^2 w_1}{\partial C_i^2}$, and $R_{12} = \frac{\partial^2 w_1}{\partial C_1 \partial C_2}$. Since it follows from Eqs. (9) and (11) that $R_{12} = 0$, while

$$R_{ii}(C_i^*) = \frac{A_i E_i - B_i D_i}{A_i B_i} \left(\frac{A_i E_i - B_i D_i}{E_i - D_i} \right)^2, \quad (13)$$

the condition $\Delta = R_{11}R_{22} > 0$ is satisfied when either R_{11} and $R_{22} > 0$ or R_{11} and $R_{22} < 0$. In the former case, $w_1(C_1, C_2)$ has a minimum at the point (C_1^*, C_2^*) , and, according to Eqs. (11) and (13), this case is realized under conditions (12a). In the latter case, $w_1(C_1, C_2)$ must have a maximum at the point (C_1^*, C_2^*) , and the conditions of its existence coincide with (12b).

If $\Delta = R_{11}R_{22} < 0$, i.e., if $R_{11} > 0$ and $R_{22} < 0$ or *vice versa*, the work $w_1(C_1, C_2)$ has no extremum at $C_1 = C_1^*$ and $C_2 = C_2^*$ (saddle point).

If conditions (12a) and (12b) are not satisfied, the values C_1^* and C_2^* do not fall within the range $(0, 1)$ and, thus, the dependence $w_1(C_1, C_2)$ is monotonic [increasing or decreasing according to the signs of derivatives (9)] along an arbitrary beam $C_2 = \alpha C_1$, where α is a positive number.

When the dependence $w_1(C_1, C_2)$ is not monotonically increasing, $w_1(C_1, C_2)$ can decrease to zero and even to negative values with increasing C_1 and C_2 under certain conditions (it is assumed that $\bar{w}_1^{(0)} > 0$). In the

general case, such an analysis is mathematically complicated for dependence (10). For this reason, we consider for simplicity the case where vacancies are in equilibrium in one of the adjacent materials, for example, in the second one; i.e., $C_2 = C_{2e}$. In this case, we have

$$\bar{w}_1(C_1) = \bar{w}_1^{(0)} + \frac{A_1}{D_1} \ln \left(\frac{1 + D_1 C_1}{1 + D_1 C_{1e}} \right) - \frac{B_1}{E_1} \ln \left(\frac{1 + E_1 C_1}{1 + E_1 C_{1e}} \right) \quad (14)$$

instead of Eq. (10). We also take

$$\Omega_1 \approx \Omega_2 = \Omega, \quad d_1 \approx b, \quad h_1 \gg 1, \quad h_{1c} \gg 1, \quad (15)$$

i.e., $A_1 \approx D_1 \approx h_1$, and $B_1 \approx E_1 \approx h_{1c}$.

Thereafter, equating expression (14) to zero for $\frac{A_1}{D_1} = \frac{B_1}{E_1} \approx 1$ and solving the resulting equation, we find that the separation work $w_1(C_1)$ vanishes for

$$C_1 = C_1^{(0)} = \frac{1 - \beta}{\beta h_{1c} - h_1}, \quad (16)$$

where

$$\beta = \frac{1 + h_1 C_{1e}}{1 + h_{1c} C_{1e}} \exp \left(-\frac{w_1^{(0)} \Omega}{bkT} \right).$$

To obtain the condition under which $0 < C_1^{(0)} < 1$,

we first estimate the quantities $\bar{w}_1^{(0)} = \frac{\bar{w}_1^{(0)} \Omega}{bkT}$ and β in the typical cases. To do this, we take into account that the adhesion-separation work w_1 for two materials can also be represented in the form [9]

$$w_1 = \gamma_1 + \gamma_2 - \gamma_{12},$$

where γ_1 , γ_2 , and γ_{12} are the surface tensions for materials 1 and 2 and at their interface, respectively. For example, from data [8] for γ_1 and γ_2 values and from our estimates [2] for γ_{12} values without vacancies, it follows that $\bar{w}_1^{(0)} \sim 1$ J/m² for the metal-metal interfaces. Then, taking $\Omega \sim 10^{-29}$ m³ and $b \approx 2-3$ Å, we obtain $\bar{w}_1^{(0)} \approx 10$ in particular for room temperatures ($kT \approx 0.025$ eV); i.e., the factor $\exp(-\bar{w}_1^{(0)}) \sim 10^{-3} \ll 1$ in Eq. (16).

At room temperatures, $C_{1e} \sim 10^{-9}-10^{-8}$, and if, for example, $h_1 C_{1e} \ll 1$ and $h_{1c} C_{1e} \ll 1$, $\beta \approx \exp(-\bar{w}_1^{(0)}) \sim 10^{-3} \ll 1$ in Eq. (16) and $C_1^{(0)} \approx \frac{1}{\beta h_{1c} - h_1}$. In this case, the inequality $0 < C_1^{(0)} < 1$ is satisfied if $\frac{h_{1c}}{h_1} > 10^3$ [here,

we take into account that $h_1 \gg 1$ according to Eq. (15)].

If $h_1 C_{1e} \ll 1$ and $h_{1c} C_{1e} \gg 1$, we have $\beta \approx \frac{10^{-3}}{h_{1c} C_{1e}} \ll 1$

and $C_1^{(0)} \approx \left(\frac{10^{-3}}{C_{1e}} - h_1\right)^{-1}$; i.e., the inequality $0 < C_1^{(0)} <$

1 is possible for $h_1 C_{1e} < 10^{-3}$. Therefore, taking into account the initial condition $h_{1c} C_{1e} \gg 1$, we obtain $h_{1c}/h_1 \gg 1$, similar to the first case.

The inequality $\frac{h_{1c}}{h_1} \gg 1$ means that the free surface of the material absorbs vacancies better than its interface with another material. In the cases considered above, this condition is necessary in order for the work of the separation of joints between a given material and another material to be reduced to zero or even to a negative value by generating a sufficient concentration of nonequilibrium vacancies in this material. In this case, the separated state of materials becomes thermodynamically more profitable than their joint.

The previous analysis shows that a similar effect ($w_1 < 0$) can be obtained by generating a certain concentration of impurity atoms in the material.

Note. We have found an inaccuracy in our previous work [4] when passing from Eqs. (10a) and (10b) to Eq. (11). Correct solutions of Eqs. (10a) and (10b) are obtained from Eqs. (12) and (15), where the coefficients of the first terms in each braces must be removed and the sign of the second term is changed to minus. The function γ_{12} is a monotonic (increasing or decreasing)

function of impurity concentrations. If γ_{12} is monotonically decreasing, it can vanish and become negative, which would correspond to the thermodynamic instability of the compound for the corresponding impurity concentrations.

REFERENCES

1. M. G. Mil'vidskii and V. B. Osvenskii, *Structural Defects in Semiconductor Single Crystals* (Metallurgiya, Moscow, 1984).
2. R. V. Gol'dshtein and M. E. Sarychev, Dokl. Akad. Nauk **380**, 476 (2001) [Dokl. Phys. **46**, 708 (2001)].
3. R. V. Goldshtein and M. E. Sarychev, Dokl. Akad. Nauk **381**, 770 (2001) [Dokl. Phys. **46**, 853 (2001)].
4. R. V. Gol'dshtein and M. E. Sarychev, Dokl. Akad. Nauk **385**, 621 (2002) [Dokl. Phys. **47**, 598 (2002)].
5. B. S. Bokshstein, N. V. Kopetskiĭ, and P. S. Shvindlerman, *Thermodynamics and Kinetics of Grain Boundaries in Metals* (Metallurgiya, Moscow, 1986).
6. J. R. Rice, in *Effect of Hydrogen on Behavior of Materials*, Ed. by A.W. Thompson and I.M. Bernstein (Metal. Soc. AIME, New York, 1976), p. 455.
7. A. M. Kosevich, *Foundations of Crystal-Lattice Mechanics* (Nauka, Moscow, 1972).
8. A. P. Babichev, I. A. Babushkina, A. M. Bratkovskii, et al., *Physical Quantities. Handbook* (Énergoizdat, Moscow, 1991).
9. A. J. Kinlock, *Adhesion and Adhesives: Science and Technology* (Chapman and Hall, London, 1987).

Translated by V. Bukhanov

TECHNICAL
PHYSICS

On the Growth Kinetics of a Single-Wall Carbon Nanotube

É. É. Lin

Presented by Academician V.E. Panin November 4, 2002

Received November 4, 2002

Until now, the formation mechanism of single-wall carbon nanotubes has remained not quite clear. The numerical modeling that was performed in [1, 2] using molecular-dynamics methods makes it possible to consider processes of synthesizing these objects at the formation stage of an open fullerene cup. However, in this case, data related to estimates of both the most probable diameter and growth time of nanotubes with formed geometry (when the nanotube length exceeds the nanotube diameter) are absent.

In this paper, we analytically solve the problem of deriving a time-dependent growth law for the average length of a formed-geometry single-wall carbon nanotube with one closed end. To that end, we use the phenomenological approach of [3, 4]. This approach allows us to describe the behavior of clusters with clearly defined collective quantum properties in stochastic conservative systems. In the given case, we deal with small carbon particles having a high characteristic frequency ν_v of carbon-atom vibrations, which is associated with a high characteristic temperature θ_v (cf., e.g., [5]) of tension vibrations of C–C chemical bonds: $2\pi\hbar\nu_v = k\theta_v$, where \hbar is the reduced Planck constant and k is the Boltzmann constant.

We below assume that the increase (growth) in the nanotube length l occurs in the process of adding nuclei to the open end. This is stipulated by the mutual compensation of free chemical bonds of both nanotube boundary atoms and atoms of a nucleus, which occurs as a result of their interaction. Plane formations, namely, carbon (graphite) hexagons, are considered as basic structure nuclei of a fullerene nanotube. The characteristic size l_0 of a nucleus can be, for simplicity, determined from the equality condition for the areas of the hexagon with the side a_0 and the circle with the radius l_0 . In accordance with [3, 4], the process of the irreversible growth of nanotubes is described by the wave $\varphi(l, t)$ of the density distribution in the space of sizes l of clusters, the wave propagating with time t

towards their increase. Then, the increase in the length l , while the nanotube diameter d remains constant, obeys the equation of a running wave in the space of l :

$$\frac{\partial\varphi(\xi, \tau)}{\partial\tau} + \Psi(\tau)\frac{\partial\varphi(\xi, \tau)}{\partial\xi} = 0. \quad (1)$$

Here, $\xi = \frac{l}{l_0}$, $\tau = \frac{t}{t_i}$, t_i is the characteristic time scale of

the nanotube–nucleus interaction and $\Psi(\tau) = \frac{d\langle\xi\rangle}{d\tau}$ is the dimensionless growth rate for the average length $\langle l \rangle$ of a nanotube. The condition of mass conservation has the form

$$M_{\text{nuc}}(t) + M_{\text{cl}}(t) = M_{\text{nuc}}(t) + \int_0^{l_{\text{max}}} \varphi(l, t)m(l, t)dl = \text{const}, \quad (2)$$

where $M_{\text{nuc}}(t)$ and $M_{\text{cl}}(t)$ are current total masses of a nucleus and a cluster, respectively, $m(l, t)$ is the cluster mass, and l_{max} is the maximum cluster size in the system. We now write out the expansion for the quantity φ in the form of the superposition of direct and backward waves:

$$\varphi(\xi, \tau) = F_1(\xi - \Psi\tau) + F_2(\xi + \Psi\tau).$$

These waves are responsible for the processes of capturing of nuclei by clusters and cluster destruction, respectively, as a result of random interactions of the objects in the system. Thus, from formulas (1) and (2), we obtain the following general form of the growth law for the average length of a nanotube in the system originally consisting of only nuclei:

$$\langle l \rangle = l_0 K \left(\frac{t}{t_i} \right)^Z. \quad (3)$$

We admit that the characteristic time scale is equal to the product of the time t_{exc} required for exciting one nucleus by the total number N of nuclei in the nanotube:

$$t_i = t_{\text{exc}} N = t_{\text{exc}} \frac{4d\langle l \rangle}{l_0^2}.$$

Russian Federal Nuclear Center,
All-Russia Research Institute of Experimental Physics,
Sarov, Nizhegorodskaya oblast, 607188 Russia
e-mail: root@gdd.vnief.ru

Here, N is determined as the ratio of the lateral-surface area of a nanotube with diameter d and length $\langle l \rangle$ to the area of a circle with diameter l_0 .

Using the relations for wave-packet broadening (see [4, 6]), we obtain from formula (3) the following expressions for the nanotube diameter and average length:

$$d = l_0^2 \sqrt{\frac{m_0}{8\hbar t_{\text{exc}}}}, \quad (4)$$

$$\langle l \rangle = \sqrt{\frac{\hbar t}{2m_0}}, \quad (5)$$

where m_0 is the nucleus mass. In analogy with quantum mechanics (see, e.g., [7, 8]), the parameter $\frac{\hbar}{2m_0}$ can be determined as the upper limit of the diffusivity in the space of the cluster sizes. Then, expression (5) is an analogue of the classical diffusion solution [9] for the growth of the new-phase particles.

We now define the parameter t_{exc} as the product of the number n of chemical bonds in a nucleus by the reciprocal characteristic frequency ν_v^{-1} of atomic oscillations in the nucleus structure, $t_{\text{exc}} = n \cdot \nu_v^{-1} = \frac{n2\pi\hbar}{k\theta_v}$.

Then, with allowance for the definition of the nucleus size, we obtain from (4) the following formula:

$$d = \frac{3\sqrt{3}a_0^2}{2\pi\hbar} \sqrt{\frac{Am_u k\theta_v}{\pi}}. \quad (6)$$

Here, A is the atomic mass and m_u is the atomic mass unit. Formula (6) involves only fundamental physical

constants and parameters of chemical bonds of carbon atoms in a nucleus and yields $d = 2.2$ nm for the value of the diameter of a single-wall carbon nanotube. This value corresponds (within an order of magnitude) to the basic experimental data presented in [1] and lies within the range 1–4 nm. This fact testifies to the adequacy of the phenomenological approach developed in the present study. From formula (5), we find that the growth time for carbon nanotubes with the average length $\langle l \rangle = 40$ nm indicated in [1] attains $t = 4 \times 10^{-6}$ s. Growth law (5) obtained by us can be useful for choosing parameters for synthesizing carbon nanotubes with a given average length.

REFERENCES

1. Yu. E. Lozovik and A. M. Popov, Usp. Fiz. Nauk **167**, 751 (1997) [Phys. Usp. **40**, 717 (1997)].
2. J. Gavillet, A. Loiseau, C. Journet, *et al.*, Phys. Rev. Lett. **87**, 275504 (2001).
3. É. É. Lin, Pis'ma Zh. Tekh. Fiz. **18**, 82 (1992) [Sov. Tech. Phys. Lett. **18**, 160 (1992)].
4. É. É. Lin, Pis'ma Zh. Tekh. Fiz. **19**, 20 (1993) [Sov. Tech. Phys. Lett. **19**, 165 (1993)].
5. Tsien Hsue Shen, *Physical Mechanics* (Peking, 1962; Mir, Moscow, 1965).
6. B. B. Kadomtsev, Usp. Fiz. Nauk **164**, 449 (1994) [Phys. Usp. **37**, 425 (1994)].
7. V. P. Dmitriev, *Stochastic Mechanics* (Vysshaya Shkola, Moscow, 1990).
8. J. P. Badiali, Phys. Rev. E **60**, 2533 (1999).
9. M. Volmer, *Kinetik der Phasenbildung* (Steinkopff, Dresden, 1939; Nauka, Moscow, 1986).

Translated by G. Merzon

Integrability of Centered Balanced Elastic Vibrations with Equal Frequencies during Free Rotation¹

S. T. Sadetov

Presented by Academician V.V. Kozlov September 9, 2002

Received August 20, 2002

New integrable mechanical systems are discovered. After Routh reduction, they allow the separation of elliptic coordinates. Solutions are obtained in terms of Riemann θ functions. The phenomenon under consideration (shift of masses in rotation) occurs in engineering.

1. Model example. Let a rigid body (“turbine”) freely rotate about an immovable vertical axis OO_1 . Let the turbine contain n smooth cylindrical cavities with rigid bodies sliding along them (Fig. 1). Let the following five conditions be satisfied.

(i) The centers of mass of the bodies can move with respect to the turbine along straight lines l_i , $i = 1, 2, \dots, n$, passing through the OO_1 axis (*centrality*).

(ii) Motion occurs in the vertical uniform gravity field with acceleration g (in the absence of other forces).

(iii) Every body is connected with the turbine by a uniform cylinder that has the axis l_i , is *linearly elastic* along l_i , and is absolutely inflexible in the transverse direction (with one degree of freedom).

(iv) For the turbine at rest, the frequencies of oscillations of bodies are equal to each other (*equality of frequencies*).

(v) The equilibrium of the system (for the conceptual absence of bases of cylindrical cavities) minimizes its moment of inertia with respect to OO_1 (*balance*).

In this case,

(a) after the *Routh reduction* with respect to the angle of rotation about OO_1 , the Lagrangian of this system has the Jacobi–Stäckel form, and the Hamilton–Jacobi equation can be separated in elliptic coordinates in \mathbf{R}^n . Hence, for the initial conditions that do not allow

impacts by bases of the cylindrical cavities, the equations of motion are Liouville integrable [1];

(b) the angular velocity squared of this rotation and the squares of the distances from bodies to the axis are expressed in terms of rational functions of *Riemann θ functions* (of n variables) and their partial derivatives of the orders $\leq n$. Its argument is the linear vector function of the new time

$$T = \int \frac{d\tau}{\mathcal{J}},$$

where τ is the input time and \mathcal{J} is the (variable) moment of inertia of the system with respect to OO_1 .

2. The derivation of the equations in the case where the damping rods are weightless and the bodies

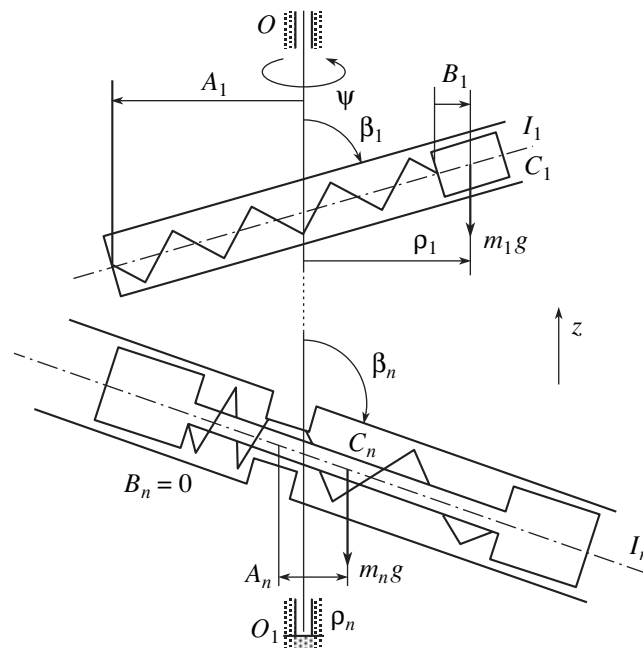


Fig. 1. Weightless springs for which $2k_i(A_i + B_i) = m_i g \sin 2\beta_i$, and k_n is the total stiffness of two (identical) springs.

¹ This article was submitted by the author in English.

move only translationally relative to the turbine. According to the *König theorem*, the kinetic energies of the turbine and the i th body have the form

$$\frac{1}{2}I_O\Psi'^2, \quad \frac{1}{2}(m_i\overrightarrow{OC_i}^2 + I_i\Psi'^2). \quad (1)$$

Here, $(\cdot)' = \frac{d}{d\tau}$ is the derivative with respect to the time τ ; Ψ is the angle of the rotation of the turbine; C_i and m_i are the center of mass and the mass of the i th body, respectively; I_O is the moment of inertia of the turbine relatively to OO_1 ; and I_i is the moment of the body relative to the axis passing through its center of mass in parallel to OO_1 .

Let ρ_i be the distance (including sign) from the center of mass C_i of the i th body to the axis OO_1 and β_i be the angle between OO_1 and l_i . Then,

$$\overrightarrow{OC_i}^2 = \frac{\rho_i^2}{\sin^2\beta_i} + \rho_i^2\Psi'^2.$$

The potential energy of the i th body has the form

$$\frac{k_i(\rho_i - B_i - A_i)^2}{2\left(\frac{\rho_i}{\sin\beta_i}\right)^2} + m_i g z_i,$$

where z_i is the vertical coordinate of the center of mass

C_i , $0 \leq \frac{B_i}{\sin\beta_i}$ is the distance from C_i to the base plane

of the rod (orthogonal to l_i) along l_i , $0 \geq \frac{A_i}{\sin\beta_i}$ is the

distance from the base plane of the rod to $l_i \cap OO_1$ along l_i , and k_i is the stiffness of the rod along l_i . In view of the relation $z_i = \rho_i \cot\beta_i$ and condition (v), this potential energy takes the form

$$\frac{k_i}{2}\left(\frac{\rho_i}{\sin\beta_i}\right)^2.$$

The Lagrangian of the turbine with oscillating bodies takes the form

$$2L = \sum_{i=1}^n \frac{m_i \rho_i^2}{\sin^2 \beta_i} + \left(I + \sum_{i=1}^n m_i \rho_i^2 \right) \Psi'^2 - \sum_{i=1}^n k_i \left(\frac{\rho_i}{\sin \beta_i} \right)^2, \quad (2)$$

where $I = I_O + \sum_{i=1}^n I_i$.

3. Reduction of rotation about OO_1 . Let $p_\Psi = \frac{\partial L}{\partial \Psi'}$

be the (constant) moment of momentum of the bundle with respect to OO_1 . Conducting the Legendre transformation with respect to Ψ' , one obtains

$$2\hat{L} = 2(L - p_\Psi \Psi') \Big|_{\Psi' \rightarrow p_\Psi} = \sum_{i=1}^n \frac{m_i \rho_i^2}{\sin^2 \beta_i} - \frac{p_\Psi^2}{I + \sum_{i=1}^n m_i \rho_i^2} - \sum_{i=1}^n k_i \left(\frac{\rho_i}{\sin \beta_i} \right)^2. \quad (3)$$

Here, $\Psi' \rightarrow p_\Psi$ denotes the expression of Ψ' from the integral of the moment of momentum.

4. Stäckel form of the Lagrangian. Let one consider the equation

$$\sum_{i=1}^n \frac{m_i \rho_i^2}{1 + \lambda \sin^2 \beta_i} = -I. \quad (4)$$

Its roots determine the elliptic coordinates in \mathbf{R}^n [2–4] (if all the angles β_i , $\pi - \beta_i$ are different and are not equal to zero, $I, m_i > 0$). They satisfy the inequalities

$$\lambda_1 < -\sin^{-2}\beta_1 < \dots < \lambda_n < -\sin^{-2}\beta_n \leq -1.$$

The following formulas are obtained from Eq. (4) by comparison of residues in λ at the points $a_i = -\sin^{-2}\beta_i$:

$$2T^{\text{rel}} = \sum_{i=1}^n \frac{m_i \rho_i^2}{\sin^2 \beta_i} = -\frac{I}{4} \sum_{i=1}^n \frac{\Gamma_i \lambda_i^2}{A(\lambda_i)}, \quad (5)$$

$$\sum_{i=1}^n \frac{k_i \rho_i^2}{\sin^2 \beta_i} = I \omega^2 \sum_{i=1}^n \Gamma_i^{-1} [(\sum a_i) \lambda_i^{n-1} - \lambda_i^n], \quad (6)$$

$$\Gamma_i = (\lambda_i - \lambda_1) \dots (\lambda_i - \lambda_n), \quad \omega = \sqrt{\frac{k_i}{m_i}},$$

$$A(w) = (w - a_1) \dots (w - a_n),$$

$$\frac{I}{I + \sum_{i=1}^n m_i \rho_i^2} = (-1)^{n-1} a_1 \dots a_n \sum_{i=1}^n \Gamma_i^{-1} \lambda_i^{-1}. \quad (7)$$

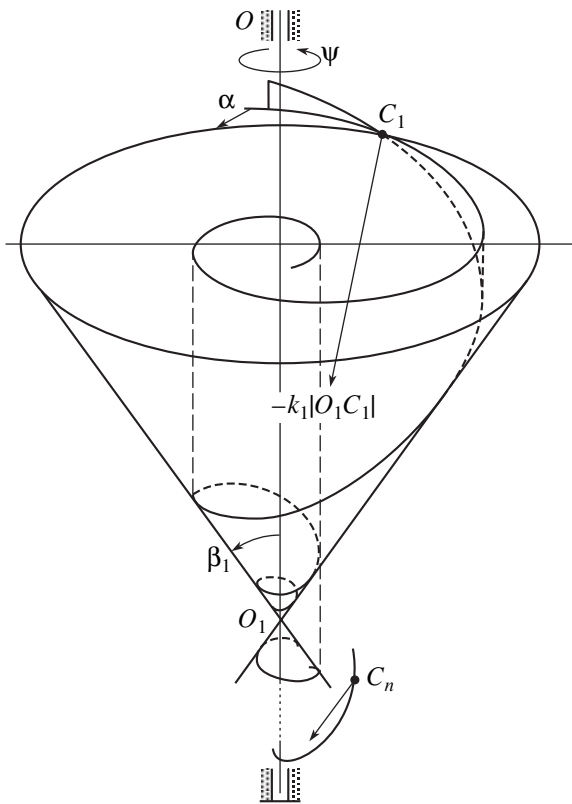


Fig. 2. Rotating system of conical logarithmic spirals.

Formulas (6) and (7) are obtained by using the expressions for

$$\sum_{i=1}^n \operatorname{res}_{w=\lambda_i} \frac{w^j}{\Lambda(w)}, \quad j = n-1, n, -1,$$

$$\Lambda(w) = (w - \lambda_1) \dots (w - \lambda_n).$$

In Eq. (7), the expression for

$$\sum_{i=1}^n \operatorname{res}_{w=a_i} \frac{w^{-1} \Lambda(w)}{A(w)}$$

is also used (cf. [6]).

Let $\mu_i = \frac{\partial T^{\text{rel}}}{\partial \lambda_i'}$ be the momenta. The fact that the

Lagrangian has the Stäckel form [1, 2] means that the corresponding Hamiltonian can be represented in the

$$\text{form } \sum_{i=1}^n \Gamma_i^{-1} H_i(\lambda_i, \mu_i).$$

5. Separation of variables [2, 3]. Let us substitute Eqs. (5), (6), and (7) into Eq. (3) and make the Leg-

endre transformation in $\lambda_1', \lambda_2', \dots, \lambda_n'$, passing to the momenta μ_i in the natural Lagrangian. Substituting $\mu_i = \frac{\partial S}{\partial \lambda_i}$

into the resulting Hamiltonian, one arrives at the Hamilton–Jacobi equation (where the coefficients of Γ_i^{-1} depend only on λ_i).

Hence, it allows a separable solution $\sum_{i=1}^n S_i(\lambda_i, F_{n-1})$, where F_{n-1} is the energy constant.

One can introduce additional $n - 1$ arbitrary constants F_0, F_1, \dots, F_{n-2} in this solution, in view of the identity

$$\sum_{i=1}^n \Gamma_i^{-1} \left(\sum_{j=0}^{n-1} F_j \lambda_i^j \right) = F_{n-1}.$$

Then, this solution is a generating function of a symplectic map (3).

The passage to the Abel–Jacobi equations and integration in θ -functions follow from [2–5, 7]. The reactions in two bearings acting on the axis (Fig. 1) are polynomials of degree ≤ 3 in $\rho_i, \rho_i', \rho_i''$.

6. Generalizations. Let Lagrangian (2) be extended by means of the parameter $\alpha = \text{const}$:

$$2\tilde{L} = \sum_{i=1}^n m_i \left((1 + \cot^2 \alpha + \cot^2 \beta_i) \rho_i'^2 - \omega^2 \frac{\rho_i^2}{\sin^2 \beta_i} \right) + \left(I_0 + \sum_{i=1}^n m_i \rho_i^2 \right) \psi'^2 + 2\psi' \left(\sum_{i=1}^n m_i \rho_i \rho_i' \right) \cot \alpha.$$

After the reduction, the Lagrangian \tilde{L} can be separated in elliptic coordinates

$$\sum_{i=1}^n \frac{m_i \rho_i^2}{1 + \lambda \cot^2 \alpha \sin^2 \beta_i} = -I_0$$

(for $\cot \alpha \neq 0$) and can be integrated in θ functions.

The Lagrangian \tilde{L} describes the motion of material points over the freely rotating, inflexibly connected system of spatial curves—conical logarithmic spirals with a common axis (Fig. 2) (here, the condition of central-

ity is weakened). The points interact with the curves by means of weightless elastic filaments (stretched along either the curves or chords).

This problem is similar to the Jacobi problem [2] of the motion of a point over the surface of an ellipsoid.

ACKNOWLEDGMENTS

I am grateful to V.V. Kozlov for discussions and Mathematische Institut, der Universität Bonn for exceptional conditions for research. This work was supported by the Deutscher Akademischer Austauschdienst (grant no. A/96/28670).

REFERENCES

1. V. I. Arnol'd, V. V. Kozlov, and A. I. Neistadt, *Current Problems of Mathematics. Fundamental Tendencies* (VINITI, Moscow, 1985), Vol. 3, pp. 5–304.
2. C. G. J. Jacobi, *Vorlesungen über Dynamik* (Druck und Verlag von G. Reimer, Berlin, 1884; ONTI, Moscow–Leningrad, 1936).
3. V. V. Kozlov, *Prikl. Mat. Mekh.* **59** (1), 3 (1995).
4. Yu. Mozer, *Usp. Mat. Nauk* **36** (5), 109 (1981).
5. V. V. Kozlov and Yu. N. Fedorov, *Mat. Zametki* **56** (3), 74 (1994).
6. S. Wojciechowcki, *Phys. Lett. A* **107** (3), 106 (1985).
7. B. A. Dubrovin, *Usp. Mat. Nauk.* **36** (2), 11 (1981).

Indentation of a Smooth Spherical Die into a Perfectly Plastic Half-Space¹

R. I. Nepershin

Presented by Academician A.Yu. Ishlinskiĭ September 16, 2002

Received September 20, 2002

A numerical model of an unsteady indentation of a smooth spherical die into a perfectly plastic half-space is given. The plastic half-space is incompressible and satisfies the full plasticity condition according to the Tresca yield criterion. The indentation load calculated as a function of the plastic-impression radius, as well as the shape of the plastic boundary near the die, agrees reasonably well with experimental data.

The axisymmetric problem of perfect-plasticity theory for the initial plastic flow of a half-space under the pressure of smooth flat and spherical dies was solved numerically in [1–3]. For the indentation of the smooth spherical die, the velocity field that satisfies the condition of nonnegative energy dissipation of the plastic flow, as well as the statically admissible continuation of the stress field into the rigid region, was given in [3, 4]. In this paper, the unsteady axisymmetric problem of the plastic flow is solved numerically for the indentation of the smooth spherical die into the incompressible perfectly plastic half-space satisfying the full plasticity condition according to the Tresca yield criterion. It is a model of the hardness test of prestrained low hardening materials by the penetration of a smooth spherical indenter. The initial stage of the indentation of the smooth spherical die agrees reasonably well with experimental data [6]. As the radius of the plastic impression increases, the experimental indentation load exceeds the theoretically predicted value due to the contact friction effect.

We consider the indentation of the smooth spherical die into the perfectly plastic half-space in the cylindrical coordinates $\{r, z, \theta\}$ associated with the die. The coordinate origin O is located at the lower point of the die. The die is fixed in these coordinates, while the half-space moves along the z axis with the unit velocity $V = 1$.

¹ This article was submitted by the author in English.

Moscow State Academy of Instrument Engineering and Informatics,
ul. Stromynka 20, Moscow, 107846 Russia

Figure 1 shows the plastic region to the right of the symmetry axis for the penetration of an R -radius die to the depth h relative to the initial contact point O of the die with the half-space. We specify the indentation stage by the contact arc angle α_A of the die with the plastic region. During die indentation, the plastic region increases from zero, and its size is comparable with the die contact length. For this reason, we use the die contact length as the unit reference length, $R\alpha_A = 1$, for calculation of the plastic region at the current indentation stage. For the whole indentation model, we use the die radius as the unit length $R = 1$. In this case, the contact arc length is α_A . Stresses are made dimensionless by dividing them by the yield stress σ_Y of the perfectly plastic material under uniaxial compression.

For the problem under consideration, the full plasticity condition, which corresponds to the edge of the Tresca prism in the space of the principal stresses, is given as

$$\sigma_1 = \sigma_2, \quad \sigma_3 = \sigma_1 - 1. \quad (1)$$

The principal stresses σ_1 and σ_3 lie in the $\{r, z\}$ plane, and $\sigma_2 = \sigma_\theta$. Under condition (1), the axisymmetric problem of perfect-plasticity theory is statically determinate and hyperbolic [3]. The characteristic curves for

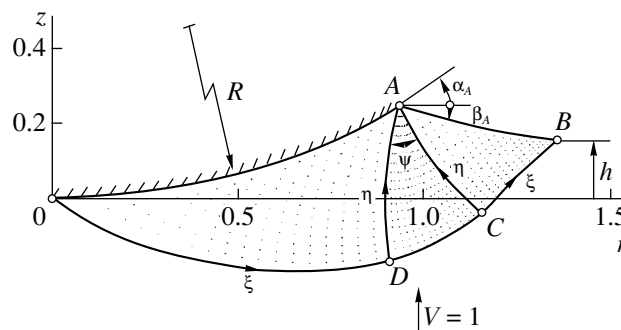


Fig. 1. Slipline field in the $\{r, z\}$ physical plane for the indentation of a smooth spherical die for the parameters $\alpha_A = 0.5236$, $h = 0.163$, $R\alpha_A = 1$.

the stresses and velocities fields coincide with the sliplines ξ and η in the $\{r, z\}$ plane:

$$\frac{dz}{dr} = \tan\varphi \text{ for } \xi \text{ and } \frac{dz}{dr} = -\cot\varphi \text{ for } \eta, \quad (2)$$

where φ is the angle between the tangent to the ξ slipline and r axis. Differential relations along the sliplines have the form

$$d\sigma - d\varphi = \frac{dr + dz}{2r} \text{ along } \xi, \quad (3)$$

$$d\sigma + d\varphi = \frac{dr - dz}{2r} \text{ along } \eta \quad (4)$$

for $\sigma = \frac{\sigma_1 + \sigma_3}{2}$ and φ and

$$dV_\xi - V_\eta d\varphi = -\frac{V_\xi dr - V_\eta dz}{2r} \text{ along } \xi, \quad (5)$$

$$dV_\eta + V_\xi d\varphi = -\frac{V_\xi dz + V_\eta dr}{2r} \text{ along } \eta \quad (6)$$

for the projections V_ξ and V_η of the velocity on the sliplines ξ and η . The velocity projections in cylindrical coordinates are related to V_ξ and V_η as

$$V_\xi = V_r \cos\varphi + V_z \sin\varphi, \quad (7)$$

$$V_\eta = V_z \cos\varphi - V_r \sin\varphi,$$

$$V_r = V_\xi \cos\varphi - V_\eta \sin\varphi, \quad (8)$$

$$V_z = V_\xi \sin\varphi + V_\eta \cos\varphi.$$

The sliplines intersect the smooth boundary OA at an angle of $\frac{\pi}{4}$. Therefore, the boundary conditions for Eqs. (2)–(4) at the die contact have the form

$$r = R \sin\alpha, \quad z = R(1 - \cos\alpha),$$

$$\varphi = \alpha - \frac{\pi}{4}, \quad R = \frac{1}{\alpha_A}, \quad 0 \leq \alpha \leq \alpha_A, \quad (9)$$

where α is the angle between the tangent to the boundary OA and the r axis. The velocity component normal to the boundary OA is equal to zero, and we have the following boundary condition for the velocities on this boundary:

$$V_\xi = V_\eta \text{ on } OA. \quad (10)$$

Velocities are continuous on the rigid–plastic boundary $ODCB$, because it is the slipline intersecting the symmetry axis at the point O . In the rigid region of the half-space, Eqs. (7) for $V_r = 0$ and $V_z = 1$ provide

$$V_\xi = \sin\varphi, \quad V_\eta = \cos\varphi \text{ on } ODCB. \quad (11)$$

The plastic material on the boundary AB is in the uniaxial-compression state $\sigma_1 = \sigma_2 = 0, \sigma_3 = -1$. The boundary AB coincides with the σ_3 direction. The sli-

plines intersect this boundary at an angle of $\frac{\pi}{4}$. Calculations of the velocity field of the initial plastic flow for the indentation of the spherical die into the half-space with a linear boundary [4] show that the velocity increases along the boundary AB from the point B to the point A . Owing to this increase, the material rises above the initial undeformed boundary of the half-space, and this behavior agrees with experiments on the penetration of a spherical indenter into a prestrained low hardening material [6]. We assume that the boundary AB is a smooth curve, where the tangent angle decreases monotonically from the maximum value β_A at the point A to zero at the point B . The boundary conditions for Eqs. (2)–(4) on AB have the form

$$\sigma = -\frac{1}{2}, \quad \varphi = \frac{\pi}{4} - \beta, \quad 0 \leq \beta \leq \beta_A, \quad (12)$$

$$\tan\beta = -\frac{dz}{dr} \text{ on } AB.$$

The boundary AB at the current indentation stage is formed by material points moved from the boundary AB of the preceding indentation stage. Therefore, the kinematic differential relation

$$\frac{ds}{V} = dh \text{ on } AB \quad (13)$$

must be satisfied on this boundary. Here, ds is the magnitude of the material-point displacement from the preceding boundary AB to the current boundary AB during the “time” increment dh , V is the magnitude of the velocity of the point, and dh is the increment of the indentation depth $h = z_B$. The volume of the spherical segment with the height h is equal to the volume of the plastic region above the boundary z_B due to the incompressibility condition. Therefore, h is related to the equation of the boundary AB as

$$h = \frac{1}{r_B^2} \left[z_A \left(r_A^2 - \frac{1}{3} z_A^2 \right) + 2 \int_A^B z r dr \right], \quad (14)$$

where $r_A = R \sin\alpha_A$ and $z_A = R(1 - \cos\alpha_A)$ are the coordinates of the point A .

The point A is the degenerate ξ slipline with a polar singularity with stresses and velocities varying in the fan angle ψ of the sliplines and with the center at the point A :

$$\psi = \frac{\pi}{2} - (\alpha_A + \beta_A). \quad (15)$$

The inequality $\psi > 0$ defines the limiting values of the contact angle α_A and the die indentation depth h for the

slipline field and the plastic region mode shown in Fig. 1. From Eqs. (3) and (12), we find

$$\sigma = -\left(\frac{1}{2} + \zeta\right), \quad \varphi = \frac{\pi}{4} - (\beta_A + \zeta), \quad (16)$$

$$0 \leq \zeta \leq \psi \text{ at the point } A.$$

The field of stresses and velocities in the plastic region must satisfy the condition

$$D = \sigma_1 \varepsilon_1 + \sigma_2 \varepsilon_2 + \sigma_3 \varepsilon_3 \geq 0$$

of nonnegative energy dissipation of the plastic flow, where $\varepsilon_1, \varepsilon_2, \varepsilon_3$ are the principal strain rates. From full plasticity condition (1) and incompressibility condition $\varepsilon_1 + \varepsilon_2 + \varepsilon_3 = 0$ for $D \geq 0$, we obtain the inequality $\varepsilon_3 \leq 0$, which means that the dissipative function D is nonnegative if the elongation rate of the linear element along the σ_3 stress trajectory is negative. For the orthogonal curvilinear coordinates connected with the directions of the principal stresses σ_3 and σ_1 , this condition takes the form

$$\varepsilon_3 = dV_3 - V_1 d\varphi \leq 0, \quad (17)$$

where the velocity projections V_3 and V_1 on the stresses

σ_3 and σ_1 are related to V_ξ and V_η as $V_3 = \frac{V_\xi - V_\eta}{\sqrt{2}}$ and

$V_1 = \frac{V_\xi + V_\eta}{\sqrt{2}}$, and $d\varphi$ is the increment of the tangent

angle to the arc element of the σ_3 stress trajectory.

The indentation of the spherical die into the perfectly plastic half-space is simulated by numerical calculations of the fields of sliplines and velocity for an increasing sequence of the contact angles α_A from zero to a finite value satisfying the inequality $\psi > 0$.

The angle β values at the N nodes of the boundary AB are specified by the parametric power function

$$\beta = \beta_A \lambda^n, \quad 1 \geq \lambda \geq 0, \quad (18)$$

with a constant step in λ , and the σ distribution over the boundary OA that satisfies the boundary condition (12) is calculated. The boundary AB is determined by the

integration of the equation $\frac{dz}{dr} = -\tan\beta$ from the

point A when solving the inverse Cauchy problem for Eqs. (2)–(4) for the N nodes specified on the boundary OA by Eqs. (9). This procedure reduces to the numerical solution of the sequence of the N nonlinear equations

$$f_1(\sigma) + \frac{1}{2} = 0, \quad (19)$$

where f_1 denotes the numerical procedure of calculating the σ value at a node on the boundary AB for a σ value specified at the node on the boundary OA along the ξ slipline. For the first node near the point A , this pro-

cedure includes the solution of the Cauchy problem from the node on the boundary OA and from the point A with $\zeta = \psi$ in Eqs. (16), the solution of the Goursat problem from the found node with specified data at the singular point A , and the solution of the inverse Cauchy problem, which determines the node of the boundary AB using differential relations (2) and (3) along the ξ slipline and the angle φ defined by Eq. (12). The difference between the σ value found at the node on the boundary AB and the value $\sigma = -\frac{1}{2}$ specified in Eq. (12)

determines the left-hand side of Eq. (19). For the next nodes of the boundary OA , the known data for the Goursat problem on the previous ξ slipline are used in the f_1 procedure. The initial σ value at the node on the boundary OA is taken to be equal to the known σ value at the preceding node. In this case, Eq. (19) is almost instantly solved numerically by Newton's method with an accuracy of 10^{-4} on a Pentium 130 computer.

When Eq. (19) is solved for the ξ slipline passing through the points O and B , the rigid-plastic boundary $O-B$, the boundary AB , and the indentation depth $h = z_B$, which is a function of the angle β_A in Eqs. (18), are determined. Then we calculate the integral on the right-hand side of Eq. (14), and difference between the right- and left-hand sides of this relation is treated as the following nonlinear equation for the angle β_A :

$$f_2(\beta_A) = 0, \quad (20)$$

which is solved by Newton's method. For the initial guess $\beta_A^0 = 0.8\alpha_A$, the rapidly convergent iterative process provides β_A values with an accuracy of 10^{-4} .

When the slipline field in the plastic region is calculated by using the static boundary conditions for σ and φ and the integral incompressibility condition (14), we calculate the velocity field by the numerical integration of Eqs. (5) and (6) with the boundary conditions (10) and (11). The mixed boundary value problem is solved in the region OAD , Goursat problems are solved in the regions ADC and ACB , and the velocities on the boundary AB are found. Kinematic relation (13) on the boundary AB is satisfied within an accuracy of $\sim 10^{-3}$ at the final stage of the die indentation for $\alpha_A = 0.5236$ with the step $\Delta\alpha_A = 0.035$, when $n \approx 0.75$ in Eq. (18). For small contact angles $\alpha_A < 0.0785$, the left- and right-hand sides of Eqs. (13) are equal to about 10^{-4} .

The slipline field in the $\{r, z\}$ plane and the velocity field in the $\{V_r, V_z\}$ hodograph plane for $\alpha_A = 0.5236$ are shown in Figs. 1 and 2, respectively. Since the velocity changes stepwise from $V_z = 1$ to $V_z = 0$ at the point O , the velocity varies almost stepwise along the ξ slipline nearest to the rigid-plastic boundary with the variable discontinuity, which is determined by integrating Eq. (5). The plastic region ABC (Fig. 1) is mapped onto the narrow segment on the velocity hodograph (Fig. 2) with the continuous decrease in the velocity V_3

along the trajectory of the principal stress σ_3 , which coincides with the boundary AB . The curvature of σ_3 trajectories is positive ($d\varphi > 0$) on the physical plane (Fig. 1). The velocity projections V_3 and V_1 are positive, and the velocity V_3 decreases along the σ_3 trajectories (Fig. 2). Inequality (17) is satisfied in the whole plastic region, and the dissipative function D is positive. The statically admissible continuation of the stress field in the rigid region for this mode of the slipline field was given in [4].

Figure 3 shows the boundaries of the plastic region for 15 steps of the die indentation up to the contact angle $\alpha_A = 0.5236$. This figure shows that the stress-free boundary AB for small α_A angles is close to the horizontal line. The slipline field in this region including the flat die with $\alpha_A = 0$, as well as the distributions of the contact normal stress, coincides with the numerical solutions of the problem for the initial plastic flow of the half-space with the horizontal boundary AB [1–4]. The difference of the numerical results is within the accuracy of calculations. With an increase in the contact angle α_A , the fan angle ψ of the slipline field decreases and approaches zero for $\alpha_A^* \approx 0.835$.

The normal pressure on the die boundary is equal to the modulus of the principal stress $|\sigma_3| = \frac{1}{2} - \sigma$. Integrating the normal pressure distribution on the contact boundary OA with the use of the relation $r = R \sin \alpha$, we determine the vertical load on the die as

$$Q = \pi R^2 \left(\frac{1}{2} \sin^2 \alpha_A - \int_0^{\alpha_A} \sigma \sin 2\alpha d\alpha \right). \quad (21)$$

The average pressures that are shared by the plastic impression area and by the spherical contact area are the dimensionless Meyer and Brinell hardness numbers, which are defined by the relations

$$q_M = \frac{Q}{\pi R^2 \sin^2 \alpha_A}, \quad q_B = \frac{Q}{2\pi R^2 (1 - \cos \alpha_A)}. \quad (22)$$

The average plastic strain ϵ_p necessary for estimation of the yield stress of the hardened material is determined by the specific work in the plastic region [5]

$$\epsilon_p = \frac{1}{V_p} \int_0^h Q dh, \quad (23)$$

where V_p is the plastic region volume for the indentation depth h .

The dimensionless values of the plastic-impression radius, indentation depth, average pressures, and average plastic strain are given in the table for various die-contact angles up to $\alpha_A = 0.7854$.

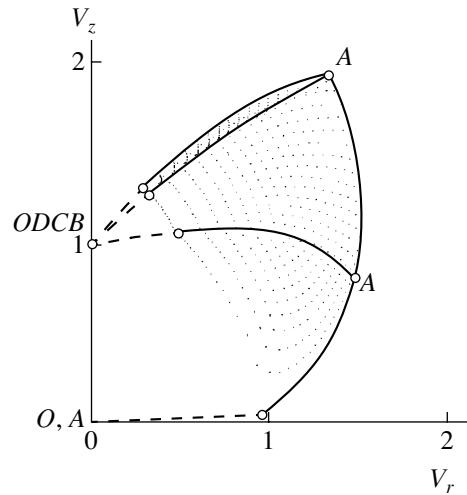


Fig. 2. Velocity hodograph of the plastic region in the $\{V_r, V_z\}$ plane for $\alpha_A = 0.5236$.

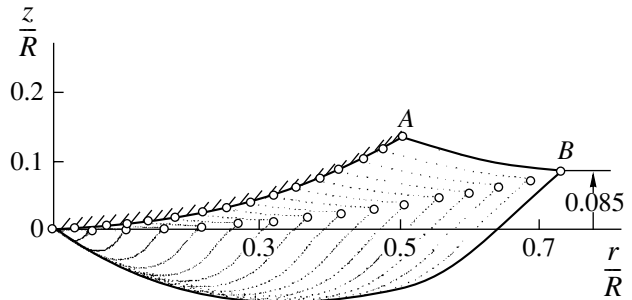


Fig. 3. Boundaries of the plastic region for 15 steps of the die loading up to $\alpha_A = 0.5236$.

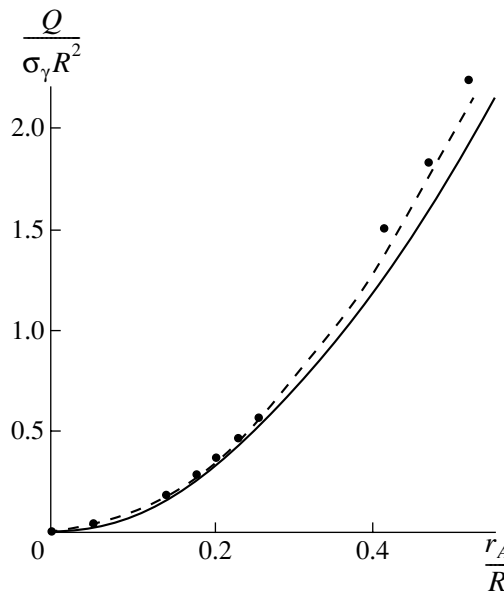


Fig. 4. Load on the smooth spherical die versus the plastic-impression radius for (solid line) this model and (dashed line) model presented in [1–4]. The experimental points for the indentation of a polished tungsten carbide ball into work-hardened copper are taken from [6].

Table

α_A	$\frac{r_A}{R}$	$\frac{z_A}{R}$	$\frac{h}{R}$	q_M	q_B	ε_p
0.0000	0.0000	0.0000	0.0000	2.814	2.814	0.0000
0.0873	0.0872	0.0038	0.0025	2.742	2.736	0.0491
0.1745	0.1736	0.0152	0.0099	2.667	2.647	0.0999
0.2618	0.2588	0.0341	0.0222	2.590	2.546	0.1516
0.3491	0.3420	0.0603	0.0390	2.512	2.436	0.2037
0.4363	0.4226	0.0937	0.0601	2.432	2.318	0.2542
0.5236	0.5000	0.1340	0.0853	2.352	2.195	0.3037
0.6109	0.5736	0.1808	0.1140	2.271	2.066	0.3520
0.6981	0.6428	0.2340	0.1460	2.192	1.935	0.3984
0.7854	0.7071	0.2929	0.1807	2.112	1.803	0.4444

The load $\frac{Q}{\sigma_Y R^2}$ calculated in this model for the indentation of the smooth spherical die as a function of the plastic-impression radius is shown in Fig. 4 in comparison with both the similar dependence obtained in [1–4] for the indentation problem with the horizontal half-space boundary and the experimental data [6]. The yield stress is found from the experimental dependence $\sigma_Y(\varepsilon_p)$ for the low work-hardening material [6] by using

the ε_p values given in the table. In the range $\frac{r_A}{R} < 0.3$, the present model results virtually coincide with experimental data and numerical results [1–4]. As the radius of the plastic impression increases, the deviation of the experimental data from this theory increases, which can be attributed to the contact friction effect ignored in the present model. The dependence obtained in [1–4] also lies above the present theoretical curve and is surprisingly close to the experimental data. The horizontal boundary of the half-space that was taken in the model [1–4], as well as the contact friction effect, is responsible for the increase in the die pressure compared with the present model.

REFERENCES

1. A. Yu. Ishlinskiĭ, *Prikl. Mat. Mekh.* **8** (30), 201 (1944).
2. A. Yu. Ishlinskiĭ, *Applied Problems of Mechanics* (Nauka, Moscow, 1986), Vol. 1, pp. 17–42.
3. A. Yu. Ishlinskiĭ and D. D. Ivlev, *Mathematical Theory of Plasticity* (Fizmatlit, Moscow, 2001).
4. D. D. Ivlev and R. I. Nepershin, *Izv. Akad. Nauk SSSR, Mekh. Tverd. Tela*, No. 4, 159 (1974).
5. B. A. Druyanov and R. I. Nepershin, *Theory of Technological Plasticity* (Mashinostroenie, Moscow, 1990).
6. O. Richmond, H. L. Morrison, and M. L. Devenpeck, *Int. J. Mech. Sci.* **16**, 75 (1974).

Mechanical Properties of Interface Layers in Polymer Matrix Composites for Large Elastic Deformations

Academician I. F. Obraztsov, Yu. G. Yanovskii, and V. É. Zgaevskii

Received October 24, 2002

The mechanical properties of polymer matrix composites are determined not only by the characteristics of a matrix, properties of a filler, and filler concentration in a material but also by the features of physicochemical interaction between different components in boundary (interface) layers. Owing to the characteristics of interaction between polymer macromolecules and the surface of the filler, interface layers have, as a rule, a complicated microstructure.

The micromechanical properties of interface layers significantly affect the formation of the macromechanical properties of a composite. Therefore, the evaluation of these micromechanical properties is of scientific interest.

In the approximation of small deformations [1], we described the micromechanical properties of an interface layer formed by macromolecules each having one end rigidly fixed (chemically bonded) to the filler surface. The results of numerical model experiments showed that the presence of a surface impermeable for macromolecule segments, as well as the steric interaction between macromolecules, which depends on their concentration on the surface, is responsible for changing the macromolecule conformations in the interface layer. It was assumed that this change is equivalent to the action of a hypothetical force depending on the properties of the surface and the physicochemical nature of the macromolecules. As the initial conformation of the macromolecules in this approximation, we took the conformation of the macromolecules far from the filler surface. In this approach, it is possible to apply the classical stress–elongation dependence, which is used in the theory of superelasticity, to describe the mechanical properties of the interface layer. In the framework of the same approach, the dependence of the Poisson's ratios of such an interface layer on the parameters characterizing the surface effect was analyzed in [2].

In this study, the mechanical properties of an interface layer in a polymer matrix composite for large (finite) elastic deformations are described in detail.

According to [1, 2], the stress tensor σ_{ls} in the interface layer is written in the form

$$\sigma_{ls} = 2C\lambda_{ln}\lambda_{sn}\alpha_{(n)}^2 - p\delta_{ls} - \sigma_{ls}^0, \quad (1)$$

where $C = \frac{T\chi R^0}{2Na^2h}$ is the analogue of the Mooney constant appearing in phenomenological superelasticity theory (T is the absolute temperature in energy units, χ is the number of the macromolecules attached to the

surface per unit area, R^0 is the rms distance between the ends of a macromolecule far from the surface, N is the number of the segments in the macromolecule, a is the linear size of a segment, and h is the thickness of the

interface layer); $\lambda_{ln} = \frac{\partial x'_l}{\partial x_n}$ (x_n and x'_l are the coordinates of a point of the interface layer before and after deformation, respectively); $\alpha_{(n)}$ is the relative change in the point coordinates in the interface layer, which is associated with the surface effect; p is the uniform pressure; δ_{ls} is the Kronecker delta; σ_{ls}^0 is the true stress caused by the fictitious surface forces; summation over repeated indices is implied; and an index standing in parentheses excludes summation.

Relation (1) is valid for an incompressible body under the condition

$$\alpha_2 = \alpha_3 = \alpha_1^{-\frac{1}{2}}. \quad (2)$$

In the coordinate system where the X_1 axis is perpendicular to the surface, the stress tensor σ_{ls}^0 has the components

$$\begin{aligned} \sigma_{11}^0 &= 2C(\alpha_1^2 - \alpha_2^2), \\ \sigma_{22}^0 &= \sigma_{33}^0 = 0, \\ \sigma_{ik}^0 &= 0, \text{ if } i \neq k. \end{aligned} \quad (3)$$

Using Eq. (1), we immediately find

$$\sigma_{11} = 2C\lambda_{1n}\lambda_{1n}\alpha_{(n)}^2 - p - \sigma_{11}^0, \quad (4)$$

$$\sigma_{12} = 2C\lambda_{1n}\lambda_{2n}\alpha_{(n)}^2 - \sigma_{12}^0, \quad (5)$$

$$\sigma_{22} = 2C\lambda_{2n}\lambda_{2n}\alpha_{(n)}^2 - p - \sigma_{22}^0, \quad (6)$$

$$\sigma_{33} = 2C\lambda_{3n}\lambda_{3n}\alpha_{(n)}^2 - p - \sigma_{33}^0, \quad (7)$$

$$\sigma_{13} = 2C\lambda_{1n}\lambda_{3n}\alpha_{(n)}^2 - \sigma_{13}^0, \quad (8)$$

$$\sigma_{23} = 2C\lambda_{2n}\lambda_{3n}\alpha_{(n)}^2 - \sigma_{23}^0. \quad (9)$$

From Eqs. (5), (8), and (9), it follows that

$$\sigma_{12} = \sigma_{21}, \quad \sigma_{23} = \sigma_{32}, \quad \sigma_{13} = \sigma_{31}.$$

For tension along the X_1 axis, the following conditions are satisfied:

$$\lambda_{22} = \lambda_{33} = \lambda_{11}^{-\frac{1}{2}}, \quad \lambda_{ik} = 0, \quad \text{if } i \neq k;$$

$$\sigma_{22} = \sigma_{33} = 0.$$

Using this relationship, substituting the p values from either (6) or (7) into Eq. (4), and taking into account Eqs. (2) and (3), we obtain the formula

$$\sigma_{11} = 2C\left[(\lambda_{11}^2 - 1)\alpha^2 + \left(1 - \frac{1}{\lambda_{11}}\right)\frac{1}{\alpha}\right]. \quad (10)$$

If the surface effect is absent ($\alpha = 1$), the relationships of the theory of superelasticity for an isotropic body follow immediately from Eq. (10).

For tension along the X_2 axis, the condition $\sigma_{11} = \sigma_{33} = 0$ is valid. Therefore, substituting Eqs. (4) and (7) into this condition and using Eq. (3), we arrive at the relation

$$\lambda_{33}^2 = \lambda_{11}^2\alpha^3 - \alpha^3 + 1. \quad (11)$$

The incompressibility condition $\lambda_{11}\lambda_{22}\lambda_{33} = 1$ and Eq. (11) provide the following relation between λ_{11} and λ_{22} :

$$\lambda_{11}^2 = \frac{1}{2\alpha^3}\left[\alpha^3 - 1 + \sqrt{(1 - \alpha^3)^2 + 4\frac{\alpha^3}{\lambda_{22}^2}}\right].$$

Next, substituting p expressed from Eq. (4) into Eq. (6), excluding λ_{11}^2 in the resulting expression, and taking into account the last relationship, we obtain the formula

$$\sigma_{22} = 2C\left(\frac{\lambda_{22}^2}{\alpha} - \frac{1}{2}\sqrt{\left(\alpha^2 - \frac{1}{\alpha}\right)^2 + 4\frac{\alpha}{\lambda_{22}^2}}\right) + C\left(\alpha^2 - \frac{1}{\alpha}\right). \quad (12)$$

According to the symmetry of the problem,

$$\sigma_{33} = 2C\left(\frac{\lambda_{33}^2}{\alpha} - \frac{1}{2}\sqrt{\left(\alpha^2 - \frac{1}{\alpha}\right)^2 + 4\frac{\alpha}{\lambda_{33}^2}}\right) + C\left(\alpha^2 - \frac{1}{\alpha}\right). \quad (13)$$

For shear deformations, when $\lambda_{nm} \neq 0$ (where n or m is equal to unity), $\lambda_{11} = \lambda_{22} = \lambda_{33} = 1$, and the remaining $\lambda_{ik} = 0$, we have

$$\sigma_{nm} = 2C\left(u_{nm}\frac{1}{\alpha} + u_{nm}\alpha^2\right), \quad (14)$$

where $u_{nm} = \frac{1}{2}(\lambda_{nm} + \lambda_{mn})$ and the antisymmetric part is equal to zero, because the moments of forces acting on a volume element of the body must be equal to zero.

When either $\lambda_{23} \neq 0$ or $\lambda_{32} \neq 0$ (at $\lambda_{11} = \lambda_{22} = \lambda_{33} = 1$ and the remaining $\lambda_{ik} = 0$), we find

$$\sigma_{23} = \sigma_{32} = 2C\frac{1}{\alpha}(\lambda_{23} + \lambda_{32}). \quad (15)$$

In accordance with Eqs. (10) and (12)–(15), the stress-tensor components of the interface layer are expressed in terms of the relative elongation and the molecular and structural characteristics of the polymer matrix as

$$\sigma_{11} = 2C\left[(\lambda_{11}^2 - 1)\alpha^2 + \left(1 - \frac{1}{\lambda_{11}}\right)\frac{1}{\alpha}\right],$$

$$\sigma_{22} = 2C\left(\frac{\lambda_{22}^2}{\alpha} - \frac{1}{2}\sqrt{\left(\alpha^2 - \frac{1}{\alpha}\right)^2 + 4\frac{\alpha}{\lambda_{22}^2}}\right) + C\left(\alpha^2 - \frac{1}{\alpha}\right),$$

$$\sigma_{33} = 2C\left(\frac{\lambda_{33}^2}{\alpha} - \frac{1}{2}\sqrt{\left(\alpha^2 - \frac{1}{\alpha}\right)^2 + 4\frac{\alpha}{\lambda_{33}^2}}\right) + C\left(\alpha^2 - \frac{1}{\alpha}\right),$$

$$\sigma_{12} = \sigma_{21} = 2C\left[\alpha^2\frac{1}{2}(\lambda_{12} + \lambda_{21}) + \frac{1}{2\alpha}(\lambda_{12} + \lambda_{21})\right],$$

$$\sigma_{13} = \sigma_{31} = 2C\left[\alpha^2\frac{1}{2}(\lambda_{13} + \lambda_{31}) + \frac{1}{2\alpha}(\lambda_{13} + \lambda_{31})\right],$$

$$\sigma_{23} = \sigma_{32} = 2C\frac{1}{\alpha}(\lambda_{23} + \lambda_{32}).$$

It is seen that the stress-tensor components are equal to zero at $\lambda_{ik} = \delta_{ik}$. When the surface effect can be

neglected ($\alpha_{(n)} \neq 1$), these relations transform to those known in the theory of superelasticity for an isotropic body. However, if the surface effect is taken into account ($\alpha_{(n)} \neq 1$), the expressions obtained above differ considerably not only quantitatively (modification of C) but also qualitatively from the relations known in the theory of superelasticity of isotropic materials, because the surface-effect factor $\alpha_{(n)}$ appears in combination with the λ_{ik} elements. In this case, large deformations in the interface layer cannot be described by introducing an effective shear modulus into the theory of superelasticity for isotropic materials, because it does not represent the actual molecular mechanism of the process.

To describe large uniaxial tensions ($\lambda_{(nn)} > 3$), we introduce the reduced relative elongations $\mu_{11} = \lambda_{11}\alpha$, $\mu_{22} = \lambda_{22}\alpha^{-\frac{1}{2}}$, and $\mu_{33} = \lambda_{33}\alpha^{-\frac{1}{2}}$ and write the expression for stress in the form

$$\sigma_{(nn)} = 2C \left(\mu_{(nn)}^2 - \frac{1}{\mu_{(nn)}} \right) \quad (16)$$

usual in the theory of superelasticity. To describe large shear deformations, we introduce the following effective constants representing the surface effect:

$$C_1 = C \left(\alpha^2 + \frac{1}{\alpha} \right), \quad C_2 = C \frac{1}{\alpha},$$

which makes it possible to formally write the standard

relationships

$$\sigma_{13} = \sigma_{31} = C_1(\lambda_{13} + \lambda_{31}),$$

$$\sigma_{12} = \sigma_{21} = C_1(\lambda_{12} + \lambda_{21}),$$

$$\sigma_{23} = \sigma_{32} = C_2(\lambda_{23} + \lambda_{32}).$$

Thus, large elastic deformations of interface layers in polymer matrix composites are described in terms of the molecular and structural characteristics of the polymer matrix. The mechanical characteristics of the interface layer are essentially determined by the behavior of macromolecules in the polymer matrix near the filler surface, which affects the conformation of the macromolecules and packing density [3]. Therefore, a uniform quantitative description of the stress-strain behavior of the structurally complicated (transversely isotropic) medium considered above is possible in terms of the material parameters C and α_n , which are found from independent numerical experiments.

ACKNOWLEDGMENTS

This work was supported by the International Science and Technology Center, project no. 2154p.

REFERENCES

1. I. F. Obraztsov, Yu. G. Yanovskii, and V. É. Zgaevskii, Dokl. Akad. Nauk **371**, 617 (2000) [Dokl. Phys. **45**, 175 (2000)].
2. I. F. Obraztsov, Yu. G. Yanovskii, A. N. Vlasov, and V. É. Zgaevskii, Dokl. Akad. Nauk **378**, 336 (2001) [Dokl. Phys. **46**, 366 (2001)].
3. V. E. Zgaevskii, Yu. G. Yanovskii, A. N. Vlasov, *et al.*, Mekh. Kompoz. Mater. Konstr. **5** (2), 109 (1999).

Translated by Yu. Vishnyakov

Cumulative Curves for Size Distributions of the Number of Defects at Different Stages of Accumulating Damages in Conditions of Fatigue and Creep

I. B. Oparina and L. R. Botvina

Presented by Academician O.A. Bannykh December 5, 2002

Received December 6, 2002

This paper deals with analysis and finding of regularities in the development of discontinuities at different stages of multiple fracture and passage to localized fracture in metallic materials. The accumulation of defects in the form of pores and microcracks in a metallic material starts from the moment of its loading. From the standpoint of the general lifetime, this stage has a decisive significance: its duration often exceeds the stage of crack propagation by an order of magnitude or more. With growing deformation, the number and size of defects gradually increase. The defects begin to merge, which in turn leads to the formation of a main crack and fracture of the material. As follows from [1], these processes result in a change of the shape of the cumulative curve for the size distribution of defects. We now analyze these distributions in order to determine the stage responsible for the initiation of merging defects in a material as a result of the process of its loading in conditions of creep and fatigue.

The analysis of processes occurring in a material under deformation is performed with the use of a function that represents the dependence of the accumulated number of defects N_{Σ} (i.e., the number of defects with a size not smaller than l) as a function of their current size l . This dependence is described by a power law of the form

$$N_{\Sigma} = Al^{-b}. \quad (1)$$

Each of the curves obeying Eq. (1) is determined by the angular coefficient b related to the lower branch of the corresponding curve ($N_{\Sigma} - l$). To find the tangents of the inclination angles for a cumulative curve, each of its segments was approximated by a straight line with the least-squares method. We now consider a variation of the exponent b in power relationship (1) with growing

deformation in conditions of creep and fatigue for various materials presented in Table 1.

It is well known that the creep of metallic materials is characterized by three stages: (I) unsteady, (II) stationary, and (III) accelerated. The most long-term stage (II) of the stationary creep preferentially corresponds to a unified fracture mechanism, namely, to the nucleation and growth of separate pores and microcracks (Fig. 1, curves 1–3). As is seen from Table 1, the inclination angle for curves of damage accumulated at the stationary stage lies within the range $5.6 \leq b \leq 14$.

In the process of the passage from the stationary stage (II) of the creep to the accelerated one (III), the reduction in the tangent b of the inclination angle of the cumulative curves begins. As is demonstrated by Table 1, this parameter decreases by a factor of 2–4 compared to its value at the stationary stage and lies within the range $3 \leq b \leq 3.8$. The decrease in the parameter b is associated with the appearance of larger

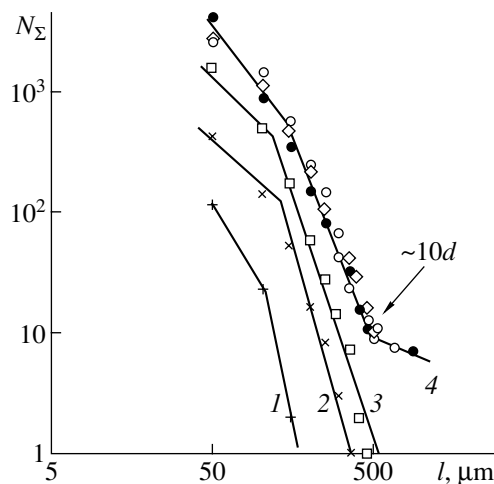


Fig. 1. Cumulative curves for the distribution of the number of wedge-shaped cracks as a function of the size of austenitic-steel (20Cr35Ni) samples [6] tested in creep conditions at the deformation rate $\dot{\epsilon} = 10^{-4} \text{ min}^{-1}$: (1) $\epsilon = 3.8\%$; (2) 5.8%; (3) 8.3%; (4) 8.4, 9.9, 12.1%.

defects formed as a result of merging of smaller defects. This leads to the displacement of the distribution curves towards continuities of a larger size. At this stage, the formation of the main crack becomes complete.

Merging of defects is enhanced at the accelerated stage (III) of the creep. At this stage, the passage to localized fracture occurs, which causes further reduction in the parameter b (Fig. 1, curve 4). This parameter now varies within the range $0.55 \leq b \leq 2$ (Table 1). In certain cases (see Table 1), at the unsteady and accelerated creep stages, values b of the inclination angles are absent. This is explained by the fact that tests were not carried through to the stage of localized fracture. Thus, the value of the angular coefficient b on the curve exhibiting the size distribution of the accumulated number of defects is a quantitative measure characterizing the passage from the stage of multiple to localized fracture.

Figure 2 shows the variation of the parameter b in the process of growth in the number and size of wedge-shaped cracks in samples of austenitic steel with enhancing deformation. As is seen from the plot, at the accelerated creep stage (compared to the stationary one), the parameter b is reduced by a factor of 9. Thus, this parameter is probably quite admissible in use as a prognostic criterion for estimation of material fracture.

Similar size distributions for the accumulated number of cracks, which are presented in Fig. 3, were obtained for laboratory samples made of carbon steel (0.2% carbon). These samples were tested in conditions of cyclic loading and at different relative lifetimes $\frac{n}{n_f}$ (the ratio of the loading-cycle number n to the number n_f of cycles leading to the sample's fracture) [7]. As is shown in Fig. 3, the variation of the relative lifetime

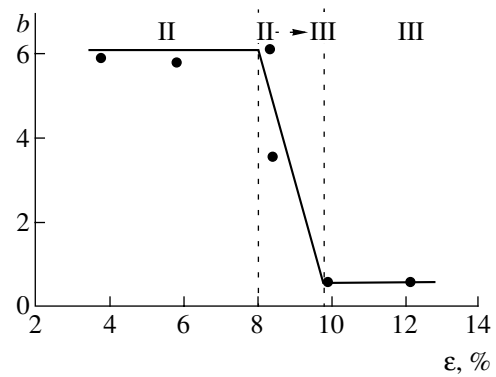


Fig. 2. Dependence of the parameter b on the degree of deformation for austenitic steel (20Cr35Ni) [6] tested for creep at the deformation rate $\dot{\epsilon} = 10^{-4} \text{ min}^{-1}$.

changes the shape of the curve connecting the total number N_{Σ} of microcracks to their size. At the initial stages, a rapid accumulation of the number of defects occurs (the upper plateau of curve 2 lies higher than the similar segment of curve 1). Furthermore (at the relative lifetime of 0.85, curve 3), the increase in the number of microcracks virtually ceases. The increase in their length due to merging of neighboring defects then begins. The onset of microcrack coalescence can be observed from the curve corresponding to the accumulated number of defects. At the relative lifetime $\frac{n}{n_f} = 0.85$ and 0.97 , this curve exhibits a break, and the inclination angle decreases (see Fig. 3 and Table 1). The reduction in the parameter b (at $\frac{n}{n_f} = 0.85$) is consistent with a decrease in the Zhurkov–Kuksenko concen-

Table 1. Values of the exponent b in relationship (1) for different creep stages

Form of testing	Material and temperature of testing	Objects under observation and their sizes	Inclination angle b at different creep stages			References
			stationary stage	unsteady stage	accelerated stage	
Creep	Al, 25°C	Aggregations, 0.4–0.8 μm	7.2; 8.2	3.8		[2]
	Fe, 70°C	Pores, 10–15 μm	5.6; 7.1; 8.3			[3]
	Steel 304, 700°C	Pores, 1–20 μm	6.7, 7.3; 6.1	3		[4]
	Cu, 405°C	Pores, 0.1–0.4 μm	12; 11.8; 13.9; 14			[5]
	Austenitic steel (20Cr35Ni), 700°C, $\dot{\epsilon} = 10^{-4} \text{ min}^{-1}$	Wedge-shaped microcracks, 100–600 μm	5.9; 5.8; 6.1	3.6	0.65	[6]
	Austenitic steel (20Cr35Ni), 700°C, $\dot{\epsilon} = 10^{-2} \text{ min}^{-1}$	Wedge-shaped microcracks, 100–600 μm	–	3.6	0.55	[6]
Fatigue	Steel (0.2%C)	Wedge-shaped microcracks, 25–600 μm	6.7	3.3	2	[7]

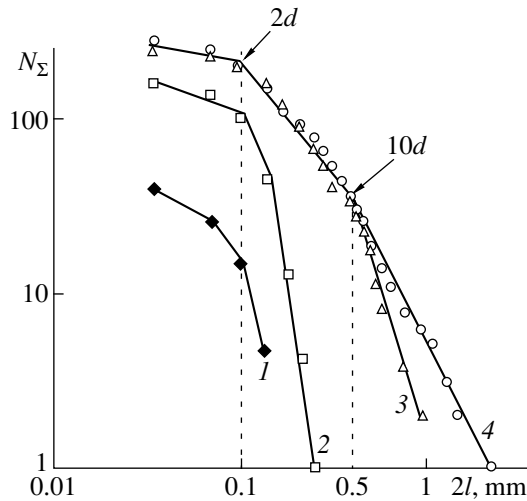


Fig. 3. Accumulated-damage curve for carbon steel [7] tested at cyclic loading in the case of stress amplitude of 333 MPa up to values of relative lifetimes: (◆) $\frac{n}{n_f} = 0.17$; (□) 0.43; (△) 0.85; and (○) 0.97.

tration parameter [8]. This parameter can be estimated according to the relationship

$$K = \frac{C^{-1/3}}{l}, \tag{2}$$

where l is the linear crack size and C is the average number of cracks per unit volume. The onset of microcrack merging corresponds to the value of the concentration criterion $K = 6-2.5$ [9]. As is clear from Table 2, at the relative lifetime $\frac{n}{n_f} = 0.85$, $K = 5.7$, which corresponds to the onset of the process of microcrack merging.

Curves of the accumulated damage (Figs. 1, 3), as a rule, consist of several linear segments. We now analyze the connection of breaks in these curves to the material structure and the critical crack size.

Table 2. Values of the exponent b in relationship (1) and of the concentration criterion K in Eq. (2) at different stages of multiple fracture of carbon steel for the stress amplitude of 333 MPa

$\frac{n}{n_f}$	$-b$	$K = \frac{C^{-1/3}}{l}$
0.17	5.3	50
0.43	6.7	13.8
0.85	3.3	5.7
0.97	2.0	3.4

The first break ($2l = 0.1$ mm) in the accumulated-damage curves (which is shown by an arrow in Fig. 3) in fatigue conditions corresponds to a preferential crack length approximately equal to the size of two grains (for the given steel, the grain size is $23 \mu\text{m}$). As was shown by metallographic studies performed in [10], the propagation depth of fatigue microcracks on sample surfaces approaches the size of one or two grains. The second break ($2l = 0.5$ mm) in curves 3 and 4 for the accumulated damage (shown by an arrow in Fig. 3) corresponds to the critical crack length. After this length has been attained, the process of defect merging in steel begins to occur. In the given case, the critical crack length is approximately equal to the size of 10 grains. This result is consistent with the conclusion of the author of [11], where it was shown for different metallic materials that fatigue cracks with a length shorter than 10 grain sizes are structurally sensitive. At the same time, longer cracks propagate in a material as in a continuum and obey the laws of linear fracture mechanics.

Similar results were also obtained in the course of the analysis of cumulative curves under creep conditions. In this case, the first break also corresponds to the preferential crack length, approximately equal to the size of one to two grains. As a result of metallographic studies of fractured samples, it was established that about 65% of wedge-shaped cracks have lengths equal to the extension of one boundary, while the maximum extension of microcracks usually does not exceed the length of 8–11 grains [12]. In Fig. 1, an arrow indicates the break in the distribution of the total number of wedge-shaped cracks as a function of their length. This break corresponds to a critical length of ~ 10 grain sizes (for the given steel, $d = 50 \mu\text{m}$). In the conditions of the high-temperature creep in metallic materials, pores but not microcracks are preferentially formed. In this case, not the size of a pore (e.g., its diameter) but the length of a chain consisting of the pores should be considered as a defect's size. This is explained by the fact that the stage of accelerated creep does not correspond to the appearance of pores with a certain size but is associated with their merging accompanied by the formation of a crack causing fracture.

The effect of the reduction in the inclination angle b_s before a strong earthquake is also observed for cumulative curves corresponding to the distribution of the number N of seismic events as a function of the magnitude M proportional to the length or area of a break in the Earth's crust [1, 13]. In this case, the curves are described by the Gutenberg–Richter formula [14], well known in seismology. This formula connects the number of seismic events with their energy:

$$\log N = A_s - b_s \log E = C_s - b_s M.$$

Here, N is the number of seismic events with an energy equal to or higher than E , M is the magnitude, and C_s is

a constant. The analysis of a multiple fracture, which was carried out for metallic samples, promotes understanding of processes occurring in the Earth's crust before a strong event.

Thus, the process of accumulation of damages at different structural levels (the size of a structural element varied by four orders of magnitude, namely, from 0.1 to 600 μm) under different loading conditions obeys unified regularities. The curves of the accumulated number of defects are described by the power relation $N_{\Sigma} = Al^{-b}$. Merging of pores and microcracks before a macrocrack has been formed results in a reduction (in the absolute value) of the exponent b entering into this relation. This is a quantity that yields a qualitative characteristic for the passage from the multiple-fracture stage to the localized-fracture stage. The critical microcrack length at the stage of the formation of a main crack attains, on the average, 10 grain sizes, whereas the maximum number of cracks has the extension of one to two grain sizes.

ACKNOWLEDGMENTS

This work was supported in part by the Russian Foundation for Basic Research, project no. 02-05-65231, and by INTAS, grant no. 01-0748.

REFERENCES

1. L. R. Botvina, I. M. Rotvaĭn, V. I. Keĭlis-Borok, and I. B. Oparina, Dokl. Akad. Nauk **345**, 809 (1995).
2. M. M. Myshlyaev, Fiz. Tverd. Tela **9** (4), 1203 (1967) [Sov. Phys. Solid State **9**, 937 (1967)].
3. B. G. Cane and G. W. Greenwood, Met. Sci. **9** (2), 55 (1981).
4. I. W. Chen, Acta Metall. **29**, 1321 (1981).
5. M. S. Yang, J. R. Weertman, and M. Roth, Scr. Metall. **18**, 543 (1984).
6. U. Lindborg, Acta Metall. **17**, 157 (1969).
7. C. M. Suh, R. Yuuki, and H. Kitagawa, Mater. Constr. (Paris) **8** (2), 193 (1985).
8. S. N. Zhurkov, V. S. Kuksenko, and A. I. Slutsker, Fiz. Tverd. Tela **11**, 296 (1969) [Sov. Phys. Solid State **11**, 238 (1969)].
9. V. A. Petrov, A. Ya. Bashkarev, and V. I. Vettegren', *Physical Foundations of Reliability of Construction Material Longevity* (Politekhnik, St. Petersburg, 1993).
10. V. S. Ivanova and V. F. Terent'ev, *The Nature of Metal Fatigue* (Metallurgiya, Moscow, 1975).
11. D. Taylor, Fatigue Fract. Eng. Mater. Struct. **5** (4), 305 (1982).
12. V. Lindborg, Acta Metall. **17**, 521 (1969).
13. W. D. Smith, Nature (London) **289**, 333 (1981).
14. B. Gutenberg and C. F. Richter, *Seismicity of the Earth* (Princeton Univ., Princeton, 1949).

Translated by G. Merzon

Mathematical Model of Salt Precipitation due to Groundwater Evaporation

G. G. Tsyarkin

Presented by Academician D.M. Klimov November 27, 2002

Received December 10, 2002

1. Full-scale observations show that intense evaporation of water in soils gives rise to the concentration of salts, which disturb ecological equilibrium and are responsible for the death of plants. The redistribution of salts in soils was studied, e.g., in [1–4].

Macroscopic transport processes in soils are usually described by using an approach based on the effective equations. In this approach, soil is treated as a complex thermodynamic system that satisfies the Onsager hypothesis on linear relations between generalized flows and generalized forces. Thus, description of transport processes reduces to the experimental determination of the matrix of coefficients of gradients of the water volume content, temperature, and other parameters determining the soil state [4–6].

An alternative approach to investigation of the flow of mixtures in porous media is based on the mechanics of multiphase media and was developed primarily for simulation of oil and gas deposits. In this approach, the laws of conservation of mass, energy, and momentum, as well as relations of equilibrium thermodynamics, are used. This approach was applied to the problems of soil mechanics, e.g., in [1–4]. A mathematical model of the groundwater evaporation and the accumulation and redistribution of a dissolved salt owing to the motion of the phase-transition front was proposed in [3]. Numerical experiments showed that intense evaporation can provide concentrations higher than the solubility of salt at local temperature, and mathematical description becomes inapplicable.

A mathematical model of salt precipitation that takes into account both the motion of the evaporation front and convective transport of a salt is proposed in this work. The mechanism of salt precipitation is illustrated for a given flow regime of the solution. The asymptotic solution of the problem is presented. In the plane of the basic parameters, the regions of existing

solutions that describe impurity accumulation in the solution and salt precipitation are presented. The precipitated salt mass is determined as a function of the filtration rate and ground-surface temperature.

2. Soil is treated as a porous medium saturated with an aqueous salt solution. Let the soil surface contact with air, where the partial pressure of a vapor is lower than the saturation pressure at local temperature. Under the thermodynamically equilibrium conditions, the partial pressure of the vapor over the water surface is equal to the saturation pressure. The difference between partial vapor pressures and, therefore, densities induces diffusion flow of vapor from the water surface to the atmosphere, which gives rise to the formation of the an evaporation front separating the regions saturated with the salt solution and air-water mixture. We assume that evaporation affect neither the given velocity of water moving towards the front nor atmospheric moisture (concentration of the water vapor) on the ground surface.

In the region of the air–vapor mixture, the following diffusion equation and Clapeyron equation for gases are valid:

$$\frac{\partial}{\partial t} \mathbf{v} - \operatorname{div} D_v \operatorname{grad} \mathbf{v} = 0, \quad (1)$$
$$P_v = \rho_v R_v T, \quad P = \rho_a R_a T, \quad \mathbf{v} = \frac{R_a P_v}{R_v P_a}.$$

We assume that the impurity in the region saturated with the salt solution is redistributed due to diffusion and convective transport:

$$m \frac{\partial}{\partial t} c + \mathbf{v} \cdot \operatorname{grad} c - \operatorname{div} m D_c \operatorname{grad} c = 0. \quad (2)$$

The heat transfer equations

$$\frac{\partial T}{\partial t} = a_{1,2} \Delta T \quad (3)$$

are valid in both the regions of (1) the solution and (2) the air–vapor mixture. Here, T is temperature; P is pressure; \mathbf{v} is the filtration rate; m is porosity; R is the

Institute for Problems in Mechanics,
Russian Academy of Sciences,
pr. Vernadskogo 101, Moscow, 117526 Russia
e-mail: tsyarkin@ipmnet.ru

gas constant; ρ is density; a is the thermal diffusivity; c is the salt concentration in the solution; and D_c and D_v are the diffusivities for the salt in water and vapor in air, respectively. Subscripts w , a , v , s , and c correspond to water, air, vapor, skeleton of the porous medium, and salt, respectively. Thus, the solution of the problem reduces to the solution of diffusion equations (1) and (2) for moisture and salt concentration, respectively, together with thermal transfer equations (3).

We assume that the following conditions of local thermodynamic equilibrium between water and vapor are satisfied at the evaporation front separating the regions of the solution and air–vapor mixture:

$$\begin{aligned} T_+ = T_- = T_*, \quad P_{v*} = F(T_* - \alpha c), \\ v_* = \frac{R_a P_{v*}}{R_v P_a}, \end{aligned} \quad (4)$$

where [7]

$$\begin{aligned} F(x) = 10^5 \exp \left[-7226.6 \left(\frac{1}{x} - \frac{1}{373.16} \right) \right. \\ \left. + 8.2 \ln \frac{373.16}{x} - 0.0057(373.16 - x) \right], \end{aligned}$$

α is the coefficient of the increase in the evaporation temperature with an increase in the impurity concentration, and the asterisk indicates that the value is taken at the front.

Porosity in the vapor–air region is the volume fraction filled with the mixture of the gases, which is determined as

$$m_- = m_0 - m_c,$$

where m_0 is the porosity of soil before salt precipitation and m_c is the volume fraction filled with the precipitated salt. In this case, the mass conservation law for water on the evaporation surface has the form

$$\begin{aligned} \left(\frac{\rho_w}{\rho_a} - \left(1 - \frac{m_c}{m_0} \right) \frac{\rho_{v*}}{\rho_a} \right) V_n \\ = \frac{v_n \rho_w}{m_0 \rho_a} + D_v \left(1 - \frac{m_c}{m_0} \right) (\text{grad} v)_{n2}. \end{aligned} \quad (5)$$

The mass conservation law for salt with allowance for precipitation at the evaporation front reduces to the form

$$\left(c_* - \frac{m_c \rho_c}{m_0 \rho_w} \right) V_n - \frac{c_*}{m_0} v_{n1} + D_c (\text{grad} c)_{n1} = 0. \quad (6)$$

For $m_c = 0$, Eqs. (5) and (6) provide the relations on the evaporation surface in the absence of salt precipitation.

The analysis of evaporation for temperatures up to 350 K [3] showed that heat absorption in the phase transition is negligible compared to the convective trans-

port, because the partial pressure of the vapor is small compared to atmospheric pressure. In this case, the conservation law at the interface takes the form

$$(\lambda \text{grad} T)_{n1} = (\lambda \text{grad} T)_{n2}, \quad (7)$$

where λ is the thermal conductivity. Relations (4)–(7) form the complete set of relations on the evaporation surface for determining the desired functions V_n , T_* , c_* , and P_{v*} (or v_*).

3. The mechanism of salt precipitation can be illustrated for the one-dimensional nonstationary evaporation process, where all quantities depend only on the distance from the ground. Let soil with temperature T_0 at the initial instant be saturated with a salt solution with the salt concentration c_0 , occupy the $z > 0$ half-space, and contact air with moisture v_a and temperature T_a . If the air moisture is less than the saturation moisture, an evaporation front is formed, propagates through soil, and separates the regions of the solution and vapor–air mixture.

We analyze the basic features of the accumulation and precipitation of the impurity by using a simple asymptotic solution. We assume that the initial and boundary values of the desired functions are constant, and that the filtration rate is a given function of the form

$$v = \frac{U_0}{\sqrt{t}}, \quad \text{where } U_0 = \text{const.}$$

We consider a self-similar

solution of the problem in the form $[V = \dot{Z}(t)]$

$$T = T(\zeta), \quad v = v(\zeta), \quad c = c(\zeta),$$

$$\zeta = \frac{z}{2\sqrt{D_c t}}, \quad Z(t) = 2\gamma\sqrt{D_c t}.$$

Solutions of Eqs. (1)–(3) can be represented in terms of the error functions, and a solution of the problem reduces to analysis of the set of transcendental equations at the evaporation front, which follow from Eqs. (4)–(7).

4. The set of transcendental equations was solved numerically for the characteristic parameters of soil components. Calculations that were carried out for a wide range of parameters indicate that two basic mechanisms are responsible for impurity accumulation. Figure 1 shows the profiles of the salt concentration for the following initial and boundary conditions in the problem of impurity accumulation near the front: $\alpha = 20$ K, $\rho_c = 2165$ kg/m³, $T_0 = 288$ K, $T_a = 310$ K, $v_a = 0$, $c_0 = 0.03$, and $m_0 = 0.3$.

It is seen that the impurity concentration, as well as the velocity of the phase-transition front, depends strongly on the rate of solution filtration to the evaporation surface. If the velocity of flow is high, the impurity is accumulated near the soil surface. Although the initial concentration is low (it corresponds to the salt concentration in seawater), the impurity concentration at

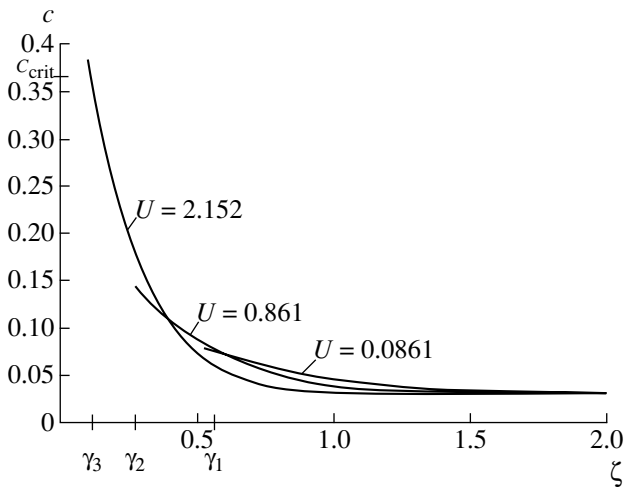


Fig. 1. Distribution of the impurity concentration accumulated ahead of the evaporation front for various filtration rates to the surface at $c_0 = 0.03$ and $v_a = 0$.

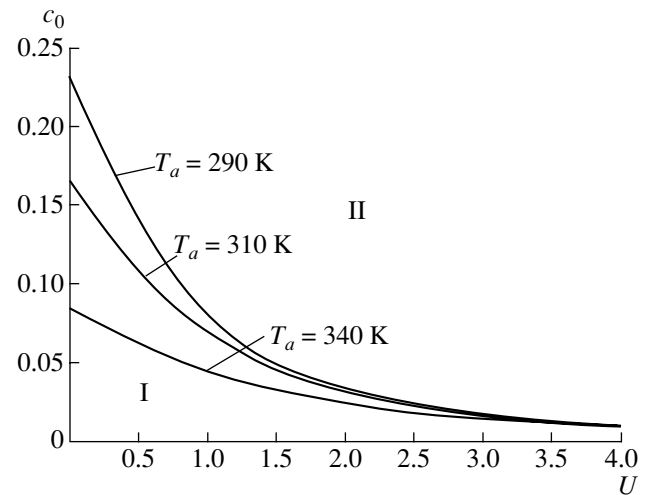


Fig. 2. Critical curves dividing the plane into regions I and II corresponding to accumulation of salts near the front and salt precipitation, respectively.

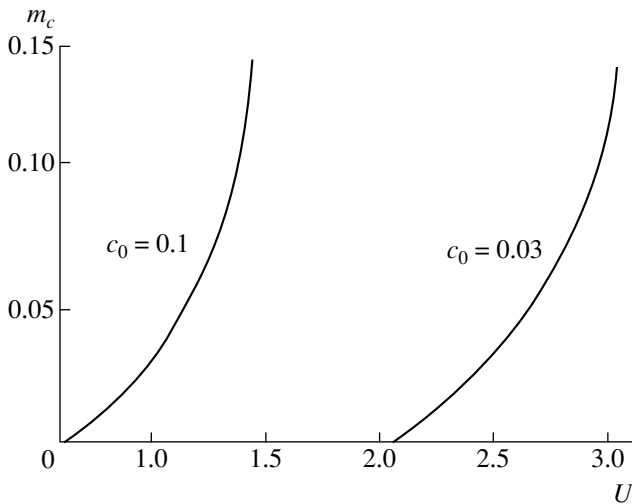


Fig. 3. Volume fraction filled with the precipitated salt vs. the rate of ground-water filtration for various initial concentrations.

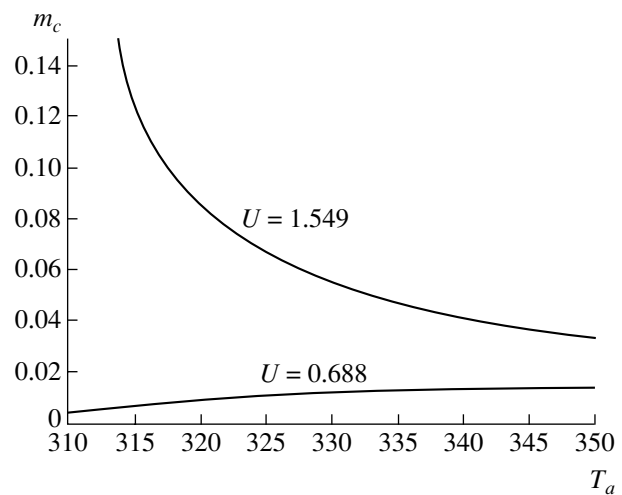


Fig. 4. Volume fraction filled with the precipitated salt vs. the temperature of the soil surface for various filtration rates of ground water.

the front for relatively high filtration rates can exceed solubility at the given temperature (line $U = 2.152$). This regime corresponds to salt precipitation.

In the (c_0, U) plane, Fig. 2 shows the critical curves separating regions I and II corresponding to salt accumulation and salt precipitation, respectively. Estimates of the characteristic quantities entering into Eq. (2)

show that the parameter $U = \frac{U_0}{m_0 \sqrt{D_c}}$ determines the

ratio of convective-to-diffusion terms. When diffusion is much slower than the convective transport, $U \gg 1$, and salts are precipitated for low initial concentrations of the solution independently of the temperature regime of soil and, therefore, of the velocity of the evaporation

front. For slow convective transport, the determining factors are the initial solution concentration and the velocity of the evaporation front, which depends strongly on the temperature of the soil surface and atmospheric moisture.

Figure 3 shows the volume fraction filled with the precipitated salt as a function of the dimensionless self-similar filtration rate U for various initial concentrations. Numerical experiments show that the sharp increase in the precipitated salt amount per unit volume is attributed to the fact that an increase in the solution filtration rate not only increases the convective transport of the impurity to the front but also suppresses the motion of the evaporation front with respect to immobile soil. In the limit case, with an increase in the solu-

tion rate, the velocity of the front vanishes, and a solution of the formulated problem does not exist, which corresponds to the filling of the porous space with the precipitated salt.

The above conclusions are illustrated by Fig. 4, which shows the temperature dependence of the precipitated salt amount for different values of the dimensionless parameter U . If the convective salt transport dominates ($U > 1$), as the surface temperature decreases, the velocity of the evaporation front decreases, and the precipitated salt amount m_c increases due to the convective salt transport to the front. If the salt diffusion prevails ($U < 1$), m_c increases with ground-surface temperature and the velocity of the evaporation front.

ACKNOWLEDGMENTS

This work was supported by the Russian Foundation for Basic Research, project no. 03-01-00068.

REFERENCES

1. R. Helmig, *Multiphase Flow and Transport Processes in the Subsurface* (Springer Verlag, Berlin, 1997).
2. C. J. Van Dajjn, L. A. Peletier, and R. J. Schotting, *Adv. Water Resour.* **22** (3), 285 (1998).
3. G. G. Tsypkin and L. Brevdo, *Transp. Porous Media* **37**, 129 (1999).
4. A. Yakirevich, P. Berliner, and S. Sorek, *Water Resour. Res.* **33** (5), 1021 (1997).
5. J. R. Phillip and D. A. de Vries, *Trans. Am. Geophys. Union* **38**, 222 (1957).
6. M. Sophocleous, *Water Resour. Res.* **15** (5), 1195 (1979).
7. M. P. Vukalovich, *Thermodynamic Characteristics of Water and Steam* (Mashgiz, Moscow, 1955).

Translated by R. Tyapaev